Monte Carlo Methods Appl. Vol. 14 No. 4 (2008), pp. 343–377
DOI 10.1515 / MCMA.2008.16

PDF modeling and simulation of premixed turbulent combustion

Michael Stöllinger and Stefan Heinz

Abstract. The use of probability density function (PDF) methods for turbulent combustion simulations is very attractive because arbitrary finite-rate chemistry can be exactly taken into account. PDF methods are well developed for non-premixed turbulent combustion. However, many real flames involve a variety of mixing regimes (non-premixed, partially-premixed and premixed turbulent combustion), and the development of PDF methods for partially-premixed and premixed turbulent combustion turned out to be a very challenging task. The paper shows a promising way to overcome this problem by extending existing PDF methods such that a variety of mixing regimes can be covered. The latter is done by a generalization of the standard scalar mixing frequency model. The generalized scalar mixing frequency model accounts for several relevant processes in addition to velocity-scalar correlations that are represented by the standard model for the mixing of scalars. The suitability of the new mixing frequency model is shown by applications to several premixed turbulent Bunsen flames which cover various regimes ranging from flamelet to distributed combustion. Comparisons to existing concepts focused on the inclusion of reaction effects in mixing frequency models for non-reacting scalars reveal the advantages of the new mixing frequency model. It is worth noting that the same methodology can be used in corresponding filter density function (FDF) methods.

Keywords. Premixed turbulent combustion, premixed stoichiometric methane-air flames, transported PDF methods, scalar mixing frequency.

1. Introduction

The extension of Reynolds-averaged Navier–Stokes (RANS) equations by probability density function (PDF) methods [3, 10, 13, 19, 41, 45, 48, 51] has significant advantages for turbulent reacting flow simulations due to the fact that there is no need to involve approximations of uncertain generality to close chemical reaction rates. The same advantage is given by the generalization of large eddy simulation (LES) methods by filter density function (FDF) methods [9, 14, 15, 16, 18, 24, 56]. FDF methods are usually more accurate but also more expensive than PDF methods [16, 20]. Due to the exact treatment of chemical reactions, the performance of PDF and FDF methods is essentially determined by the modeling of the transport of scalars (e.g., species mass fractions and temperature). Such scalar transport models involve two ingredients: a scalar mixing frequency model that determines the characteristic time scale of mixing, and a scalar mixing model that describes the change of the PDF of a scalar [13, 16, 19, 51].

Most of the previous applications of PDF and FDF methods were related to simulations of non-premixed turbulent combustion. In this case, the characteristic length and time scales of scalar fields are usually larger than the characteristic length and time scales of turbulent motions. Correspondingly, the scalar mixing frequency can be assumed to be controlled by the frequency of large-scale turbulent motions. The performance of scalar mixing models for non-premixed turbulent combustion is relatively well investigated [13, 17, 36, 37, 59]. Mitarai et al. [37] compared predictions of different mixing models to the results of direct numerical simulation (DNS). Merci et al. [32, 33, 34, 35] and Xu and Pope [62] studied various scalar mixing models in turbulent natural gas diffusion flames. The FDF method also has been successfully applied to non-premixed flames by Raman et al. [53] and Sheiki et al. [55].

Applications of PDF and FDF methods to premixed turbulent combustion are more complicated than calculations of non-premixed turbulent combustion. The appearance of fast flamelet chemistry may result in very thin reaction zones such that scalar mixing can take place on scales which are much smaller than all scales of turbulent motions [2, 29, 39, 49]. Correspondingly, there exist only a few applications of PDF methods to premixed flames. To overcome problems of earlier approaches, Mura et al. [39] recently suggested a PDF model where the outer parts of the flame structure (reactant side and product side) are described by a standard scalar mixing model whereas the inner part (the reaction zone) is described by a flamelet model. However, this approach is complicated and related to several questions (e.g. regarding the matching of both combustion regimes). The scalar mixing frequency is provided via a transport equation for the scalar dissipation rate which involves effects of chemical reactions in corresponding equations for non-reacting scalars. The model of Mura et al. [39] requires the adjustment of six parameters to the flow considered, the modeling of the dissipation rate of non-reacting scalars does not agree with many other models [54], and there are questions regarding the inclusion of chemical reaction effects (see Section 7). More recently, Lindstedt and Vaos [29] and Cha and Trouillet [6, 7] developed models that relate the scalar mixing frequency of reacting scalars to the characteristic frequency of turbulent motions and the scalar mixing frequency of non-reacting scalars, respectively. Both approaches use flamelet ideas in conjunction with several other assumptions: e.g., the assumption of a local equilibrium between production and dissipation in the scalar dissipation rate equation [29], and the assumption of local homogeneity and isotropy [6, 7]). The investigations reported here reveal that these assumptions are not satisfied in general.

The paper will address the questions described in the preceding paragraph in the following way. Section 2 deals with a description of the PDF modeling approach. The modeling of molecular scalar mixing is the concern of Section 3. The problems related to the use of the standard model for scalar mixing will be described, and a generalization of the standard mixing frequency model will be presented. The following sections describe applications of the generalized mixing frequency model to simulations of

three premixed turbulent Bunsen flames which cover various regimes ranging from flamelet to distributed combustion. The flames considered are discussed in Section 4, and the flame simulations are described in Section 5. Section 6 presents simulation results obtained with the scalar mixing frequency model introduced in Section 3 in comparison to measurements. Comparisons with modeling approaches applied previously will be discussed in Section 7. Section 8 deals with conclusions of this work.

2. The modeling approach

The modeling approach will be developed on the basis of PDF equations (which can be used as FDF equations if the ensemble averages involved are replaced by corresponding spatially filtered variables [19, 20]). The derivation of the transport equation for the joint PDF $F_\theta(\boldsymbol{\theta};\boldsymbol{x},t)$ of a number N_s of scalars (e.g., species mass fractions and temperature) can be found in a variety of textbooks. The PDF transport equation obtained reads [10, 13, 19, 51]

$$\frac{\partial \langle\rho\rangle F_\theta}{\partial t}+\frac{\partial \langle\rho\rangle \overline{u}_i F_\theta}{\partial x_i}=-\frac{\partial \langle\rho\rangle \overline{u_i^{''}|\boldsymbol{\theta}} F_\theta}{\partial x_i}-\sum_{\alpha=1}^{N_s}\frac{\partial}{\partial\theta_\alpha}\left(\langle\rho\rangle \overline{\frac{D\phi_\alpha}{Dt}|\boldsymbol{\theta}}\, F_\theta\right). \quad (1)$$

Here, $\langle\rho\rangle$ is the ensemble averaged mass density. A Favre decomposition $u_i=\overline{u}_i+u_i^{''}$ is used for velocities. Favre decompositions of other variables will be represented in the same way, this means $\overline{Q}$ refers to the mass-density averaged mean of any variable Q, and the corresponding Favre fluctuation is $Q^{''}=Q-\overline{Q}$. The sum convention is used throughout this paper for repeated Roman subscripts but not for Greek subscripts. $\overline{u_i^{''}|\boldsymbol{\theta}}$ and $\overline{\frac{D\phi_\alpha}{Dt}|\boldsymbol{\theta}}$ denote conditional Favre averages, where $\boldsymbol{\theta}$ is the sample space scalar vector. According to the Navier–Stokes equations, the substantial derivatives $\frac{D\phi_\alpha}{Dt}$ of scalars are given by

$$\frac{D\phi_\alpha}{Dt}=\frac{1}{\rho}\frac{\partial}{\partial x_k}\left(\frac{\rho\nu}{Sc_\alpha}\frac{\partial\phi_\alpha}{\partial x_k}\right)+S_\alpha. \quad (2)$$

Here, ν denotes the kinematic viscosity, Sc_α is the Schmidt number of scalar α, and S_α is a source rate due to chemical reactions. By adopting relation (2), the scalar PDF transport equation (1) can be written

$$\frac{\partial \langle\rho\rangle F_\theta}{\partial t}+\frac{\partial \langle\rho\rangle \overline{u}_i F_\theta}{\partial x_i}=\frac{\partial}{\partial x_k}\langle\rho\rangle\left[\frac{\overline{\nu}}{Sc_\alpha}\frac{\partial F_\theta}{\partial x_k}-\overline{u_i^{''}|\boldsymbol{\theta}}F_\theta\right]-\sum_{\alpha=1}^{N_s}\frac{\partial}{\partial\theta_\alpha}\langle\rho\rangle\left[M_\alpha^{''}+S_\alpha\right]F_\theta. \quad (3)$$

The only assumptions used in the derivation of the latter equation are $\nu=\overline{\nu}$ and $\overline{\partial Q/\partial x_k}=\partial\overline{Q}/\partial x_k$, where Q refers to any fluctuating variable. The molecular mixing term $M_\alpha^{''}$ in (3) is given by

$$M_\alpha^{''}=\frac{1}{F_\theta}\sum_{\beta=1}^{N_s}\frac{\partial}{\partial\theta_\beta}\left(\frac{\overline{\nu}}{Sc_\alpha}\overline{\frac{\partial\phi_\alpha}{\partial x_k}\frac{\partial\phi_\beta}{\partial x_k}|\boldsymbol{\theta}}F_\theta\right). \quad (4)$$

$M_\alpha^{''}$ is written as a Favre fluctuation because expression (4) reveals that the mean of $M_\alpha^{''}$ disappears,

$$\overline{M_\alpha^{''}} = 0. \tag{5}$$

By multiplying equation (3) with the corresponding variables and integrating over the scalar sample space, one finds for scalar means $\overline{\phi}_\alpha$ and scalar variances $\overline{\phi_\alpha^{''2}}$ the transport equations

$$\frac{\bar{D}\overline{\phi}_\alpha}{\bar{D}t} = \frac{1}{\langle\rho\rangle}\frac{\partial}{\partial x_k}\langle\rho\rangle\left(\frac{\overline{\nu}}{Sc_\alpha}\frac{\partial\overline{\phi}_\alpha}{\partial x_k} - \overline{u_k^{''}\phi_\alpha^{''}}\right) + \overline{S}_\alpha, \tag{6}$$

and

$$\frac{\bar{D}\overline{\phi_\alpha^{''2}}}{\bar{D}t} = \frac{1}{\langle\rho\rangle}\frac{\partial}{\partial x_k}\langle\rho\rangle\left(\frac{\overline{\nu}}{Sc_\alpha}\frac{\partial\overline{\phi_\alpha^{''2}}}{\partial x_k} - \overline{u_k^{''}\phi_\alpha^{''2}}\right) - 2\overline{u_k^{''}\phi_\alpha^{''}}\frac{\partial\overline{\phi}_\alpha}{\partial x_k} - 2\varepsilon_\alpha + 2\overline{S_\alpha^{''}\phi_\alpha^{''}}. \tag{7}$$

Here, $\bar{D}/\bar{D}t = \partial/\partial t + \overline{u}_k\,\partial/\partial x_k$ refers to the mean Lagrangian time derivative, and the scalar dissipation rate ε_α is given by

$$\varepsilon_\alpha = \frac{\overline{\nu}}{Sc_\alpha}\overline{\frac{\partial\phi_\alpha^{''}}{\partial x_k}\frac{\partial\phi_\alpha^{''}}{\partial x_k}}. \tag{8}$$

The definition (4) of $M_\alpha^{''}$ determines a relationship between the molecular mixing term $M_\alpha^{''}$ and scalar dissipation rate ε_α,

$$\overline{M_\alpha^{''}\phi_\alpha^{''}} = -\varepsilon_\alpha - \frac{\overline{\nu}}{Sc_\alpha}\frac{\partial\overline{\phi}_\alpha}{\partial x_k}\frac{\partial\overline{\phi}_\alpha}{\partial x_k}. \tag{9}$$

By replacing ε_α in the scalar variance equation (7) according to relation (9) one obtains a relation between $\overline{M_\alpha^{''}\phi_\alpha^{''}}$ and the transport of scalar variances which will be used below for the modeling of $M_\alpha^{''}$.

The approach applied implies the need to parametrize the conditional turbulent scalar flux $\overline{u_i^{''}|\boldsymbol{\theta}}$. This flux will be modeled by the usual gradient diffusion assumption [10, 13, 19, 51],

$$\overline{u_i^{''}|\boldsymbol{\theta}}\,F_\theta = -\frac{\nu_t}{Sc_t}\frac{\partial F_\theta}{\partial x_i}. \tag{10}$$

Here, Sc_t refers to a constant turbulent Schmidt number and $\nu_t = C_\mu k\tau$ denotes the turbulent viscosity: k is the turbulent kinetic energy, τ is the dissipation time scale of turbulence, and C_μ is a dimensionless parameter. Expression (10) for the conditional turbulent scalar flux implies the usual gradient-diffusion models for the turbulent scalar flux and turbulent scalar variance flux,

$$\overline{u_i^{''}\phi_\alpha^{''}} = -\frac{\nu_t}{Sc_t}\frac{\partial\overline{\phi}_\alpha}{\partial x_i}, \quad \overline{u_i^{''}\phi_\alpha^{''2}} = -\frac{\nu_t}{Sc_t}\frac{\partial\overline{\phi_\alpha^{''2}}}{\partial x_i}. \tag{11}$$

For simplicity, we will assume that $Sc_\alpha = Sc_t$. The resulting transport equation for the scalar PDF is then given by

$$\frac{\partial \langle\rho\rangle F_\theta}{\partial t} + \frac{\partial \langle\rho\rangle \overline{u}_i F_\theta}{\partial x_i} = \frac{\partial}{\partial x_i} \langle\rho\rangle \left(\frac{\overline{\nu} + \nu_t}{Sc_t} \frac{\partial F_\theta}{\partial x_i} - \sum_{\alpha=1}^{N_s} \frac{\partial}{\partial \theta_\alpha} \langle\rho\rangle \left(M_\alpha'' + S_\alpha\right) F_\theta. \quad (12)$$

Equation (12) implies for scalar means the equation

$$\frac{\bar{D}\overline{\phi}_\alpha}{\bar{D}t} = \frac{1}{\langle\rho\rangle} \frac{\partial}{\partial x_k} \langle\rho\rangle \left(\frac{\overline{\nu} + \nu_t}{Sc_t} \frac{\partial \overline{\phi}_\alpha}{\partial x_k}\right) + \overline{S}_\alpha. \quad (13)$$

By adopting relation (9) for ε_α, the scalar variance equation implied by equation (12) reads

$$\frac{\bar{D}\overline{\phi_\alpha''^2}}{\bar{D}t} = \frac{1}{\langle\rho\rangle} \frac{\partial}{\partial x_k} \left(\langle\rho\rangle \frac{\overline{\nu} + \nu_t}{Sc_t} \frac{\partial \overline{\phi_\alpha''^2}}{\partial x_k}\right) + 2\frac{\overline{\nu} + \nu_t}{Sc_t} \frac{\partial \overline{\phi}_\alpha}{\partial x_k} \frac{\partial \overline{\phi}_\alpha}{\partial x_k} + 2\overline{M_\alpha'' \phi_\alpha''} + 2\overline{S_\alpha'' \phi_\alpha''}. \quad (14)$$

3. Molecular mixing modeling

The scalar PDF transport equation (12) is unclosed as long as the molecular mixing term M_α'' is not specified. The latter can be done in a variety of ways [10, 13, 19, 51]. We will use a parametrization of M_α'' according to the interaction-by-exchange-with-the-mean (IEM) mixing model [11, 61],

$$M_\alpha'' = -\frac{C_\alpha}{2\tau} \phi_\alpha''. \quad (15)$$

The model (15) represents the standard mixing model which is used in most simulations of turbulent reacting flows [13, 51]. The reason for that is given by the simplicity of the model (15). The model (15) contains two ingredients: a scalar mixing model that describes changes of scalar values, and a scalar mixing frequency model that determines the characteristic time scale of mixing. The scalar mixing is modeled by $-\phi_\alpha''$, which corresponds to the idea that scalar fluctuations ϕ_α'' tend to disappear (scalar values ϕ_α tend to relax to their mean value $\overline{\phi}_\alpha$). The scalar mixing frequency $\omega_\alpha = C_\alpha/(2\tau)$ is modeled in proportionality to the mixing frequency $1/\tau$ of large-scale turbulent motions, where C_α is a nondimensional parameter. The consideration of the relatively simple standard mixing model (15) represents a natural first step of investigations of the performance of improved models for the mixing frequency ω_α in M_α'' models [21]. Justification for this approach arises from the observation that the problem considered requires, first of all, an improved modeling of the scalar mixing frequency $\omega_\alpha = C_\alpha/(2\tau)$ (see the discussion in the introduction). The question of whether the use of other scalar mixing models may further improve simulation results will be the concern of future efforts.

Expression (15) requires the definition of C_α in order to specify the scalar mixing frequency $\omega_\alpha = C_\alpha/(2\tau)$. The scalar mixing frequency ω_α determines, first of all, the evolution of the scalar variance. Thus, the equation for scalar variances represents the natural basis for the definition of C_α. By adopting expression (15) in equation (14), the scalar variance equation can be written

$$e_\alpha = P_\alpha - C_\alpha B_\alpha. \tag{16}$$

Here, B_α is given by $B_\alpha = \overline{\phi_\alpha''^2}/\tau$, and e_α and P_α are given by the expressions

$$e_\alpha = \frac{\bar{D}\overline{\phi_\alpha''^2}}{\bar{D}t} - \frac{1}{\langle\rho\rangle}\frac{\partial}{\partial x_k}\left(\langle\rho\rangle\,\frac{\overline{\nu}+\nu_t}{Sc_t}\frac{\partial\overline{\phi_\alpha''^2}}{\partial x_k}\right) - 2\overline{S_\alpha''\phi_\alpha''}, \tag{17}$$

$$P_\alpha = 2\frac{\overline{\nu}+\nu_t}{Sc_t}\frac{\partial\overline{\phi}_\alpha}{\partial x_k}\frac{\partial\overline{\phi}_\alpha}{\partial x_k}. \tag{18}$$

Equation (16) can be used to find an appropriate constant value for C_α on the basis of DNS data. The latter can be done, for example, by adopting Overholt and Pope's DNS data of passive scalar mixing in homogeneous isotropic stationary turbulence with imposed constant mean scalar gradient [42]. For the flow considered one finds that $e_\alpha = 0$, this means there is a local equilibrium between the production P_α and dissipation $C_\alpha B_\alpha$ of scalar variances, $P_\alpha = C_\alpha B_\alpha$. Overholt and Pope's DNS data then provide $C_\alpha = (1.8; 2.1; 2.2)$ for Taylor-scale Reynolds numbers $Re_\lambda = (28; 52; 84)$, respectively (these C_α values were obtained without using the gradient-diffusion approximation (11) for the turbulent scalar flux). An analysis of the Reynolds number dependence of C_α indicates a value $C_\alpha = 2.5$ for infinitely high Taylor-scale Reynolds numbers [19]. Based on these findings, the standard model for C_α is given by the use of a constant value $C_\alpha \approx 2$ for C_α [13, 19, 51]. However, a constant value of C_α means that the turbulent velocity and scalar fields are strongly correlated such that the scalar mixing frequency $\omega_\alpha = C_\alpha/(2\tau)$ is completely controlled by the frequency $1/\tau$ of large-scale turbulent motions. There is, however, no guarantee that a constant value for C_α represents a reasonable approximation for flows which are more complex than homogeneous isotropic and stationary turbulence. For example, the use of a constant value for C_α appears to be inappropriate if the characteristic time and length scales of scalar fields are found below the corresponding scales of turbulent motions, which is a characteristic feature of premixed turbulent combustion. Correspondingly, several attempts have been made to overcome the limitations of using a constant value for C_α [27, 29, 38]. Unfortunately, all these approaches presented previously are faced with significant problems: see the detailed discussion provided in Section 7. To overcome the problems related to the use of a constant value for C_α, an attempt to generalize the standard model for C_α will be made in the following.

The basic idea of the approach applied is the following one. In extension of the standard model for C_α one may assume that e_α is small compared to P_α and $C_\alpha B_\alpha$ in (16), this means one assumes that relation (16) can be basically characterized by a local equilibrium between the production P_α and dissipation $C_\alpha B_\alpha$ of scalar variances. Such an approach is often used, for example, for the derivation of algebraic stress models [13, 19, 51]. In other words, e_α may be seen as a relatively small deviation from a local equilibrium between P_α and $C_\alpha B_\alpha$. On this basis, C_α can be calculated by the constraint to minimize the deviation e_α from the local equilibrium. What is the most convenient way to formulate such a constraint for the calculation of C_α? C_α depends on e_α, P_α, and B_α according to relation (16). The calculation of e_α, P_α, and B_α in terms of simulation results will be affected by numerical errors due to the discretization of equations and the finite number of particles involved in the Monte Carlo simulation. Thus, e_α, P_α, and B_α calculated in this way represent fluctuating variables. The most convenient way to calculate C_α under these conditions is to minimize the averaged squared deviations $\langle e_\alpha^2 \rangle_T$ from the local equilibrium between production and dissipation of scalar variances (see the detailed explanations below). Here, $\langle Q \rangle_T$ refers to a temporal average of any variable Q. This idea of calculating C_α has some similarity with the calculation of the dynamic Smagorinsky coefficient in LES [51]. However, there is a problem related to this approach. The production P_α results from the modeling of velocity-scalar correlations $\overline{u_k'' \phi_\alpha''}$: see equations (7) and (11). Thus, the assumption of minimal deviations from a local equilibrium between the production and dissipation of scalar variances means that the mixing of scalars is controlled by the turbulent velocity field. This condition cannot be considered to be satisfied for premixed combustion where the characteristic mixing time scale may well be smaller than the characteristic time scales of the velocity field. Indeed, the application of this approach to the flame simulations described below leads to poor results for the F3 and F2 flames as compared to measurements, and it leads to a global extinction of the F1 flame in simulations.

Thus, the idea discussed in the preceding paragraph will be modified by considering a generalized local equilibrium between the production and dissipation of scalar variances. The term $2\overline{S_\alpha'' \phi_\alpha''}$ due to chemical reactions accounts for a correlation between scalar mixing and chemical reactions which may well be relevant in addition to velocity-scalar correlations. Therefore, the term $2\overline{S_\alpha'' \phi_\alpha''}$ will be added to the relevant terms P_α and $C_\alpha B_\alpha$ on the right-hand side of (16). To evaluate the relevance of the second term on the left-hand side of (16), it is helpful to split this term into two contributions,

$$\frac{1}{\langle \rho \rangle} \frac{\partial}{\partial x_k} \left(\langle \rho \rangle \frac{\overline{\nu} + \nu_t}{Sc_t} \frac{\partial \overline{\phi_\alpha''^2}}{\partial x_k} \right) = \frac{\overline{\nu} + \nu_t}{Sc_t} \frac{\partial^2 \overline{\phi_\alpha''^2}}{\partial x_k^2} + \frac{1}{\langle \rho \rangle \, Sc_t} \frac{\partial \langle \rho \rangle \left(\overline{\nu} + \nu_t \right)}{\partial x_k} \frac{\partial \overline{\phi_\alpha''^2}}{\partial x_k}. \quad (19)$$

The first contribution on the right-hand side of (19) can be combined with the production P_α on the right-hand side of (16). However, the relevance of the last term in

(19) seems to be low because there is no reason to expect a systematic effect on the turbulent mixing of scalars. Indeed, the simulation results reported below show that the modification of the first term on the right-hand side of (19) due to the last term is less than 5%. Thus, the last term of (19) will be added to the terms of minor relevance on the left-hand side of (16). Correspondingly, the scalar variance equation (16) can be written

$$E_\alpha = A_\alpha - C_\alpha B_\alpha. \tag{20}$$

Here, B_α is again given by $B_\alpha = \overline{\phi_\alpha''^2}/\tau$, and E_α and A_α are given by the expressions

$$E_\alpha = \frac{\bar{D}\overline{\phi_\alpha''^2}}{\bar{D}t} - \frac{1}{\langle\rho\rangle\, Sc_t} \frac{\partial \langle\rho\rangle \left(\overline{\nu} + \nu_t\right)}{\partial x_k} \frac{\partial \overline{\phi_\alpha''^2}}{\partial x_k}, \tag{21}$$

$$A_\alpha = 2\frac{\overline{\nu} + \nu_t}{Sc_t} \left(\frac{\partial \overline{\phi}_\alpha}{\partial x_k} \frac{\partial \overline{\phi}_\alpha}{\partial x_k} + \frac{1}{2} \frac{\partial^2 \overline{\phi_\alpha''^2}}{\partial x_k^2} \right) + 2\overline{S_\alpha'' \phi_\alpha''}. \tag{22}$$

It is worth noting that equation (20) represents an exact rewriting of the scalar variance equation (16). The notion of representing the scalar variance equation in terms of relation (20) is to combine the relevant processes on the right-hand side. The term E_α then represents deviations from the local equilibrium between production processes and dissipation. As explained above, the calculation of E_α, A_α, and B_α by simulation data results in fluctuating variables E_α, A_α, and B_α due to the effects of the discretization of equations and the finite number of particles involved in the Monte Carlo simulation.

Equation (20) represents the basis for the calculation of C_α. In particular, C_α will be chosen such that the averaged quadratic error

$$\left\langle E_\alpha^2 \right\rangle_T = \left\langle A_\alpha^2 \right\rangle_T - 2C_\alpha \left\langle A_\alpha B_\alpha \right\rangle_T + C_\alpha^2 \left\langle B_\alpha^2 \right\rangle_T \tag{23}$$

will become minimal. $\langle Q \rangle_T$ refers again to the temporal average of any variable Q. By analyzing $\left\langle E_\alpha^2 \right\rangle_T$ as a function of C_α one finds that

$$C_\alpha = \frac{\langle A_\alpha B_\alpha \rangle_T}{\langle B_\alpha^2 \rangle_T} \tag{24}$$

minimizes the averaged quadratic error $\left\langle E_\alpha^2 \right\rangle_T$. The difference between the standard model assuming a constant value for C_α and the C_α model (24) is given by the fact that the model (24) provides local C_α values which minimize the deviations from the local equilibrium between production processes and dissipation of scalar variances. In addition to velocity-scalar correlations, the model (24) also accounts for velocity-variance correlations (given by the second term in the parentheses expression of (22)) and scalar-reaction correlations (given by the $2\overline{S_\alpha'' \phi_\alpha''}$ term in (22)). Thus, the model (24) will be referred to below as generalized correlation (GC) model. The performance of this modeling concept in simulations will be discussed in the following sections in comparison to other C_α models.

4. The flames considered

The turbulent premixed F3, F2, and F1 flames studied experimentally by Chen et al. [8] are considered to investigate the performance of the PDF modeling approach described in Sections 2 and 3. The three highly stretched stoichiometric methane-air flames cover a range of Reynolds and Damköhler numbers. Based on an order of magnitude analysis Chen et al. [8] found that all three flames are located in the distributed reaction zones regime [44]. In particular, the F1 flame is located at the borderline to the well stirred reactor regime, and the F3 flame is located at the borderline to the flamelet regime. This wide range of combustion conditions is often found in spark ignition engines [1] which present one of the most important applications involving premixed turbulent combustion. Due to the simple configuration, the broad range of combustion conditions, and the high quality experimental database [8], the three flames considered are well appropriate to investigate the performance of PDF methods for premixed turbulent combustion.

The three flames are generated with the same burner. Table 1 presents the mean nozzle exit velocities, the corresponding Reynolds numbers, and the centerline turbulent kinetic energy values. The burner design is shown schematically in Figure 1.

Flame	F1	F2	F3
Equivalence ratio	1.0	1.0	1.0
Reynolds number	52500	40300	24200
U_0 [m/s]	65	50	30
k_0 [m^2/s^2]	12.7	10.8	3.82

Table 1. Global operating characteristics of the F3, F2, and F1 flames [8]. The Reynolds number Re is calculated on the basis of the nozzle diameter $D = 12\,\text{mm}$ and bulk velocity U_0. k_0 denotes the centerline turbulent kinetic energy at the nozzle exit.

The burner consists of a nozzle with diameter $D = 12\,\text{mm}$ for the main stream which is surrounded by a large pilot stream to stabilize the turbulent main jet flame. The laminar pilot stream is generated by an array (1165 holes of diameter 1 mm) of small jets issued through a cooled perforated plate. Both streams consist of a stoichiometric methane-air mixture (equivalence ratio $\Phi = 1$). The burner is surrounded by air at rest. The outer air is entrained into the three flames at axial positions 3D–5D, changing the flame brush to non-perfectly premixed. The experimental database includes radial profiles of the mean velocity, the turbulent kinetic energy, mean and variance of the temperature, and the mean mass fractions of the major species CH_4, O_2, CO_2, H_2O and minor species CO, H_2, OH. The error in the measurements of the mean velocity is estimated to be less than 1%, and the error of the mean temperature

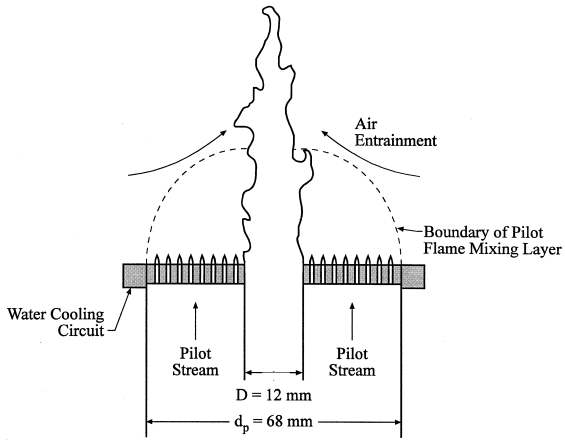

Figure 1. The burner design.

is expected to be less than 10%. The error in the measurements of the major species is between 8% to 15%, and the error regarding the minor species is within 20% to 25%.

The flames considered have been studied numerically by using different combustion models. Prasad and Gore [52] solved RANS equations. The averaged reaction rate was closed with a flame surface density model which is valid under flamelet conditions [47]. Therefore, only the F3 flame has been investigated. Herrmann [22] investigated all three flames using a modified level set approach [45] that accounts for the effects of the instantaneous flame structure and the entrainment of cold ambient air. The model is strictly valid only under flamelet conditions. Pitsch and De Lageneste [46] formulated the level set concept for LES of premixed flames and performed a F3 flame simulation. They reported issues regarding the strong influence of boundary conditions in their LES. Concerns include the significant heat losses due to the cooled burner surface, which are estimated to reach up to 20% in the pilot flame.

The PDF method was applied first by Mura et al. [39] to simulate the F3 and F2 flames. They showed that the IEM mixing model [11, 61] combined with the standard model $\omega_\alpha = 1/\tau$ for the scalar mixing frequency is inapplicable to the two premixed flames close to the flamelet regime. The use of the standard model corresponds to the idea that the scalar mixing frequency is controlled by the inertial range turbulent motions. This assumption is valid for distributed combustion, but in the flamelet regime the mixing process is controlled by the laminar flame length scale. Mura et al. [39] suggested a PDF model where the outer parts of the flame structure (reactant side and product side) are described by a standard mixing model and the inner part (reac-

tion zone) by a flamelet model. The scalar mixing frequency is provided by means of a transport equation for the scalar dissipation rate. The latter equation was obtained under the assumption of infinitely high Reynolds number and flamelet combustion conditions. More recently, Lindstedt and Vaos [29] applied the transported PDF model approach to F1, F2, and F3 flame simulations. They demonstrated the applicability of the transported PDF model approach to premixed turbulent combustion in the flamelet regime under the condition that the modeling of the scalar mixing frequency is modified. They closed the molecular mixing term by using the modified coalescence-dispersion (CD) mixing model [23]. Comparisons of results obtained with different constants $C_\alpha = 2, 4, 6, 8$ and a scalar mixing frequency model depending on the ratio of the laminar flame velocity to the Kolmogorov velocity were performed. The latter model will be referred to as Lindstedt–Vaos (LV) model. By assuming 10% heat loss for the pilot flame, a stably burning F1 flame was obtained by adopting a constant $C_\alpha > 4$. However, by assuming 20% heat loss for the pilot flame, flame extinction occurred over a wide range of constant C_α values. The latter problem did not appear by using the LV model, this means the LV model enabled stable F1 flame simulations for the case of 20% heat loss. Although the results obtained by Lindstedt and Vaos are encouraging, one has to see that the LV model involves flamelet ideas in conjunction with assumptions that are not satisfied in general (for example, the assumption of a local equilibrium between production and dissipation in the scalar dissipation rate equation). Thus, the generality of the closures applied remains to be established [29].

5. Flame simulations

A hybrid PDF-RANS approach was used to simulate the turbulent premixed flames described in Section 4. RANS equations were used for the calculation of the velocity field. The conservation of mass and momentum equations applied are given by [51]

$$\frac{\partial \langle\rho\rangle}{\partial t} + \frac{\partial \langle\rho\rangle \overline{u}_i}{\partial x_i} = 0, \tag{25}$$

$$\frac{\bar{D}\langle\rho\rangle\overline{u}_i}{Dt} = -\frac{\partial p}{\partial x_i} + \frac{\partial}{\partial x_j}\left[\langle\rho\rangle\,\bar{\nu}\left(\frac{\partial \overline{u}_i}{\partial x_j} + \frac{\partial \overline{u}_j}{\partial x_i} - \frac{2}{3}\frac{\partial \overline{u}_k}{\partial x_k}\delta_{ij}\right)\right] - \frac{\partial \langle\rho\rangle \overline{u_i'' u_j''}}{\partial x_j}. \tag{26}$$

The Reynolds stress required to close equation (26) is given by a linear stress model,

$$\overline{u_i'' u_j''} = \frac{2}{3}k\delta_{ij} - \nu_t\left(\frac{\partial \overline{u}_i}{\partial x_j} + \frac{\partial \overline{u}_j}{\partial x_i} - \frac{2}{3}\frac{\partial \overline{u}_k}{\partial x_k}\delta_{ij}\right). \tag{27}$$

The turbulent viscosity ν_t is given by the usual parametrization

$$\nu_t = C_\mu \frac{k^2}{\varepsilon}. \tag{28}$$

According to the realizable $k-\varepsilon$ turbulence model [57], the turbulent kinetic energy k and dissipation rate ε of turbulent kinetic energy are calculated by the equations

$$\frac{\bar{D}\langle\rho\rangle k}{Dt} = \frac{\partial}{\partial x_j}\left[\langle\rho\rangle\left(\bar{\nu}+\frac{\nu_t}{\sigma_k}\right)\frac{\partial k}{\partial x_j}\right] + \langle\rho\rangle C_\mu S^2\frac{k^2}{\varepsilon} - \langle\rho\rangle\varepsilon, \tag{29}$$

$$\frac{\bar{D}\langle\rho\rangle \varepsilon}{Dt} = \frac{\partial}{\partial x_j}\left[\langle\rho\rangle\left(\bar{\nu}+\frac{\nu_t}{\sigma_\varepsilon}\right)\frac{\partial \varepsilon}{\partial x_j}\right] + \langle\rho\rangle C_1 S\varepsilon - \langle\rho\rangle C_2\frac{\varepsilon^2}{k+\sqrt{\nu\varepsilon}}. \tag{30}$$

$S=\sqrt{2S_{ij}S_{ij}}$ is the magnitude of the mean rate-of-strain tensor. The model parameters are given in Shih et al. [57] and Table 2. It is worth noting that C_μ and C_1 are no constants here.

Simulation tools	Settings
Domain	Axisymmetric
Solver	Steady, segregated with implicit formulation
Turbulence model	Realizable $k-\varepsilon$ model [57] with C_μ, C_1
	defined in [57], $C_2=1.79$, $\sigma_k=1.0$, $\sigma_\varepsilon=1.2$
Turbulent Schmidt number	$Sc_t=0.5$ for F3 and F2, $Sc_t=0.6$ for F1
Wall treatment	Low Reynolds number model [12]
Discretization schemes	Presto for pressure
	PISO for pressure-velocity coupling
	Second order upwind for momentum, k and ε
Mixing model	Mix. model (15) combined with different ω_α models
Chemistry model	DRM22
ISAT parameters	ODE error tol. $=10^{-8}$, $\varepsilon_{\text{tol}}=5\cdot10^{-4}$
Particles per cell	50

Table 2. Numerical simulation data.

The scalar PDF transport equation (12) was closed with the mixing model (15) combined with the model (24) for C_α. The PDF transport equation (12) was solved by Monte Carlo simulation. The corresponding equations for particle positions x_i^* and particle scalars ϕ_α^* (species mass fractions and sensible enthalpy) are given by [13, 19]

$$dx_i^* = \left(\tilde{u}_i + \frac{1}{\langle\rho\rangle\, Sc_t}\frac{\partial\langle\rho\rangle\,(\nu_t+\overline{\nu})}{\partial x_i}\right)dt + \sqrt{\frac{2(\nu_t+\overline{\nu})}{Sc_t}}dW_i, \tag{31}$$

$$d\phi_\alpha^* = -\omega_\alpha(\phi_\alpha^* - \overline{\phi}_\alpha)dt + S_\alpha(\boldsymbol{\phi})dt. \tag{32}$$

Here, dW_i denotes the increment of the ith component of a vectorial Wiener process. The increments dW_i are Gaussian random variables which are determined by their first two moments,

$$\langle dW_i \rangle = 0, \quad \langle dW_i dW_j \rangle = \delta_{ij} dt. \tag{33}$$

The scalar mixing frequency is defined by $\omega_\alpha = C_\alpha / 2\tau$. C_α is calculated according to the GC model (24) for the fuel (CH_4) mass fraction because combustion takes place only if fuel is available. A numerical limit $\overline{\phi''^2_\alpha} \geq 10^{-6}$ was applied to avoid the calculation of unphysically high values for C_α in regions where the scalar variance $\overline{\phi''^2_\alpha}$ becomes very small. Temporally averaged variables involved in the calculation of C_α (24) were obtained by a moving average over 50 iterations. In this way, the solution of the RANS equations (25)–(30) provides the mean velocity $\overline{u}_i$, turbulent viscosity ν_t and turbulence time scale $\tau = k/\varepsilon$. These variables are then used to solve the particle equations (31)–(32). The mean density $\langle \rho \rangle$ and mean viscosity $\bar{\nu}$ are calculated from the particle compositions and temperatures and fed back into the RANS equations.

The steady-state RANS equations were discretized by the finite volume method. Details can be found in Table 2. The particle equations (31)–(32) are solved numerically by a mid-point rule [4] in order to achieve second order accuracy in time. The time step is determined from a local time stepping procedure [40]. Mean values of scalar quantities are calculated by a weighted summation over particles in a cell. For example, the term $\overline{S''_\alpha \phi''_\alpha}$ was calculated by a summation $\sum_{i=1}^{N_p} S_\alpha(\boldsymbol{\phi}^{*i})(\phi^{*i}_\alpha - \overline{\phi}_\alpha)$ over all N_p particles in a cell. The number of particles per cell is set to 50. A higher number of particles per cell was found to have no effect on simulation results. The statistical error is further reduced by averaging over the last 200 iterations [40]. All computations presented have been performed by using the FLUENT code [12].

The chemical reaction rates $S_\alpha(\boldsymbol{\phi})$ were provided by a skeletal chemical mechanism DRM22 [26] consisting of 23 species (H_2, H, O, O_2, OH, H_2O, HO_2, H_2O_2, CH_2, $CH_2(S)$, CH_3, CH_4, CO, CO_2, HCO, CH_2O, CH_3O, C_2H_2, C_2H_3, C_2H_4, C_2H_5, C_2H_6, N_2) and 104 elemental reaction. The suitability of the DRM22 mechanism will be demonstrated in Section 6 by comparisons with results obtained with the full GRI-2.11 mechanism [58]. The composition change due to chemical reactions was treated by the *in situ* adaptive tabulation (ISAT) method developed by Pope [50].

The equations were solved on a 2-dimensional axisymmetric domain. The domain extends up to $20D$ downstream (axial direction) from the nozzle exit plane and $6.5D$ in radial direction to allow entrainment of the ambient air. Here, D refers to the nozzle diameter. The domain is discretized into 220×70 (axial by radial) cells. The grid is non-uniform to improve the accuracy of computations in the flame region. The grid independence of the solution has been checked by comparison with results obtained on a 260×100 grid.

The boundary conditions applied are described in Table 3. The profiles for the axial velocity and turbulent kinetic energy at the jet inlet have been taken from the experimental database of Chen et al. [8]. The profile for the turbulent dissipation rate

Stream	Condition	Values
Jet inlet	Axial velocity U [m/s^{-1}]	Measured profiles [8]
	k [m^{2}s^{-2}]	Measured profiles [8]
	ε [m^{2}s^{-3}]	$\varepsilon = (2k/3)^{3/2}/l_{\text{lat}}$; measured l_{lat}
	T [K]	298
	Y_{CH_4}	0.0552
	Y_{O_2}	0.2201
Pilot flame	Axial velocity U [m/s^{-1}]	1.32
	k [m^{2}s^{-2}]	10^{-3}
	ε [m^{2}s^{-3}]	0.1
	T [K]	1785
	Y_{O_2}	$5 \cdot 10^{-4}$
	$Y_{\text{H}_2\text{O}}$	0.1236
	Y_{CO_2}	0.15
	Y_{CO}	$7.8 \cdot 10^{-4}$
	Y_{H_2}	$3 \cdot 10^{-5}$
	Y_{OH}	$1.2 \cdot 10^{-4}$
Rim	Adiabatic wall	
Air inlet	Pressure inlet	
Lateral boundary	Pressure outlet	
Outflow	Pressure outlet	

Table 3. Boundary conditions for the flame simulations.

has been calculated from the profile of the turbulent kinetic energy and measurements of the lateral length scale l_{lat} by adopting the relation $\varepsilon = (2k/3)^{3/2}/l_{\text{lat}}$ [8]. The pilot composition was calculated from the chemical equilibrium of a stoichiometric methane-air mixture with 20% heat loss.

To reduce the computational time, the simulations were performed in two steps. First, a laminar flame model [12] was used to generate realistic initial conditions for PDF simulations. The PDF simulations were then initialized with the results from the laminar flame model. Such a use of realistic initial conditions increases significantly the convergence rate of PDF simulations. The computations have been performed parallel on four 2.8GHz Opteron processors each equipped with 4GB of SDRAM. The computational time required for a converged solution (involving approximately 30 000 iteration steps) was about 15 hours.

6. Simulation results

Radial profiles of the normalized mean axial velocity U/U_0 are presented in Figure 2 at different axial positions $h = x/D$. The mean axial velocity $U = \overline{u}_1$ is normalized by the bulk velocity $U_0 = 30, 50, 65$ m/s for the F3, F2, and F1 flames, respectively. The overall agreement between simulation results and measurements is excellent.

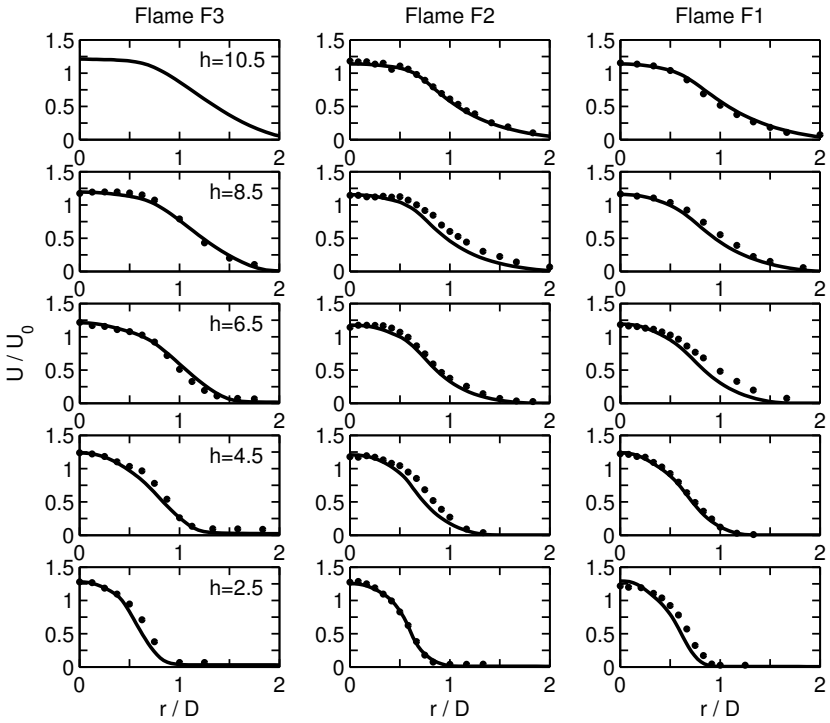

Figure 2. Normalized mean axial velocities U/U_0 for the F3, F2, and F1 flames. Dots denote experimental results [8], and lines denote simulation results.

The thermal expansion within the turbulent jet can be recognized by the increase of the axial velocity at radial positions $r/D > 0.5$ along the x-axis for all three flames. As a result of this expansion, the shear layer (which is roughly located at the position of the maximum gradient of the mean axial velocity) is pushed outward in radial direction. This trend can also be seen in Figure 3 where radial profiles of the normalized turbulent kinetic energy k/k_0 ($k_0 = 3.82, 10.8, 12.7$ m^2/s^2 for the F3, F2, and F1 flames, respectively) are shown. The peaks of the turbulent kinetic energy k are shifted outward for increasing axial positions. The results for the higher Reynolds number F2

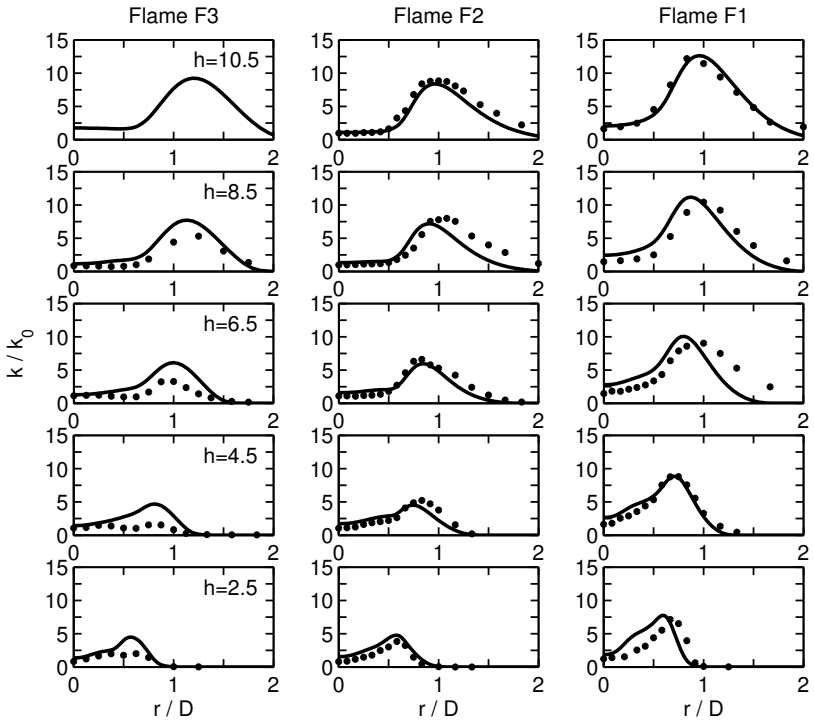

Figure 3. Normalized turbulent kinetic energy k/k_0 for the F3, F2, and F1 flames. Dots denote experimental results [8], and lines denote simulation results.

and F1 flames agree very well with the measurements whereas an overprediction of the turbulent kinetic energy can be seen regarding the F3 flame, especially close to the burner head. Similar overpredictions have been reported by Lindstedt and Vaos [29]. The F3 flame was also studied by Pitsch and de Lageneste [46] by using LES in combination with a level set approach. Their turbulent kinetic energy results show a better agreement at $h = 2.5$ but a similar disagreement at $h = 6.5$. The F3 flame has the lowest axial velocity and the highest temperature. Thus, low Reynolds number effects which are not accounted for in the $k - \varepsilon$ model applied may be the reason for the turbulent kinetic energy overprediction. Radial profiles of the turbulence Reynolds number $Re_t = k\tau/\overline{\nu}$ are shown in Figure 4 at two axial positions for the three flames considered.

Here, $\tau = k/\epsilon$ is the characteristic time scale of large-scale turbulent motions, and $\overline{\nu}$ is the mean molecular viscosity. The results are shown in radial direction until the flow becomes laminar. The profiles of Re_t are qualitatively very similar for all three flames since they are generated with the same burner.

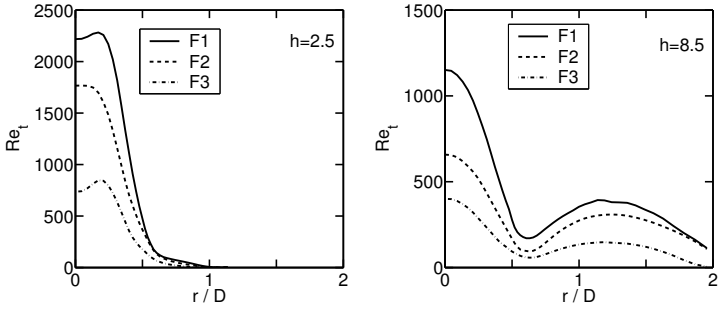

Figure 4. Radial profiles of the turbulence Reynolds number $Re_t = k\tau/\overline{\nu}$ for the F1 (solid line), F2 (dashed line) and F3 (dashed-dotted line) flames at axial positions $h = 2.5$ and $h = 8.5$.

Quantitatively, the turbulence Reynolds number of the F1 flame is about three times larger than that of the F3 flame. For a cold round jet one would expect a peak of Re_t in the shear layer. Regarding the flames considered, the high temperature in the shear layer drastically increases the molecular viscosity. The relatively high viscosity then implies the monotonic decrease of Re_t at $h = 2.5$ and the local minima observed in the Re_t profiles at $h = 8.5$. The appearance of small Re_t values in the flame brush due to a high viscosity (relaminization) is a well known phenomenon. These small Re_t values may explain the differences between simulation results and turbulent kinetic energy measurements regarding the F3 flame: most turbulence models have been developed under the assumption of high Re_t values.

Figure 5 shows radial profiles of the mean reaction progress variable $C = (\overline{T} - T_u)/(T_b - T_u)$ [8] at different axial positions for the three flames considered. Here, $\overline{T}$ is the mean temperature, $T_b = 2248$ K is the adiabatic flame temperature and $T_u = 298$ K is the temperature of the surrounding air. The simulation results of the F3 flame agree very well with the measurements. This agreement indicates that the new GC frequency model is well applicable to flamelet conditions. The F2 and F1 flame simulation results show an overprediction of the progress variable at $h = 2.5$. Lindstedt and Vaos [29] found a similar overprediction in their F1 flame simulations using the same pilot inlet conditions. A reason for the observed overprediction of the temperature close to the burner exit regarding the F2 and F1 flames could be given by the complex interaction between the turbulent jet and laminar pilot stream. Such flow conditions are rather difficult to predict within the RANS framework. LES results for the F2 and F1 flames could clarify whether this is indeed the reason for the observed overprediction. However, such LES results have not been reported so far. Possibly, a better agreement between simulation results and measurements may be obtained by adopting refined inlet conditions (e.g., a reduction of the pilot inlet temperature regarding the F2 and F1 flames).

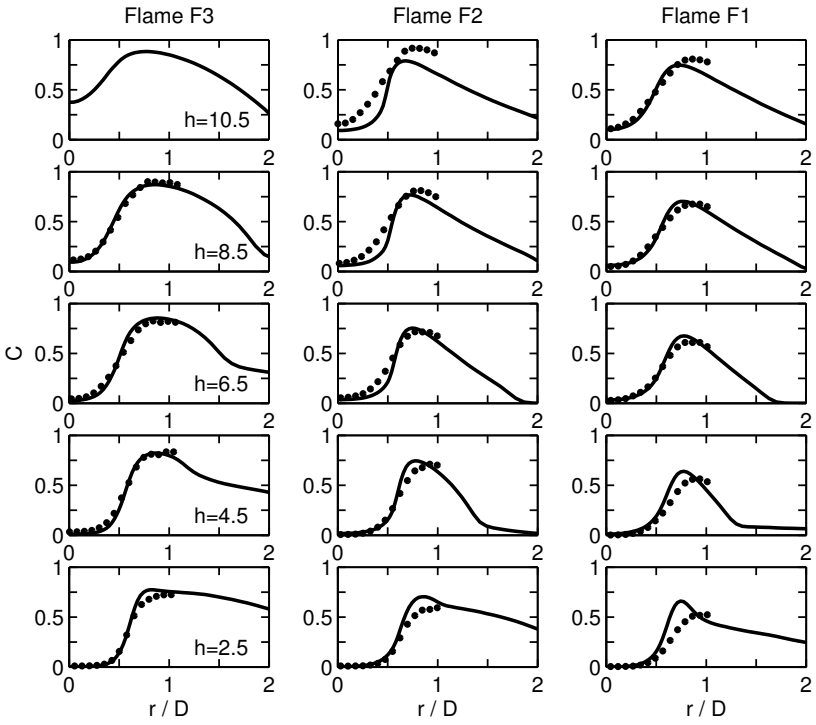

Figure 5. Mean reaction progress variable C for the F3, F2, and F1 flames. Dots denote experimental results [8], and lines denote simulation results.

Figure 6 shows simulation results of the mean oxygen mass fraction Y_{O_2}, and Figure 7 shows simulation results of the mean fuel (methane) mass fraction Y_{CH_4} for the three flames considered. Both oxygen and fuel concentrations are well predicted in all three flames. The entrainment of surrounding air is clearly visible in Figure 6. It is most intense in the highest Reynolds number F1 flame due to the high turbulence intensity. Mean mass fractions of the product species Y_{H_2O} and Y_{CO_2} are shown in Figures 8 and 9, respectively. The H_2O concentration results agree very well with the measurements for all three flames. The CO_2 concentration of the F3 flame is also well predicted whereas the F2 and F1 flame results display a slight CO_2 underprediction. Figure 10 presents radial profiles of the mean CO mass fraction Y_{CO}. This figure shows for all three flames a significant overprediction of CO which increases downstream. This finding could explain the underprediction of the CO_2 concentration in the F2 and F1 flames: the slightly too high temperature levels in the F2 and F1 flame simulations imply high CO levels and a corresponding slower oxidation of CO to CO_2.

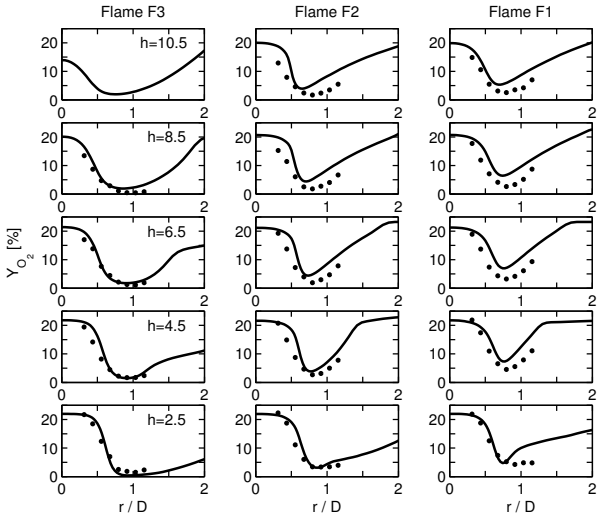

Figure 6. Mean O_2 mass fraction Y_{O_2} in percent for the F3, F2, and F1 flames. Dots denote experimental results [8], and lines denote simulation results.

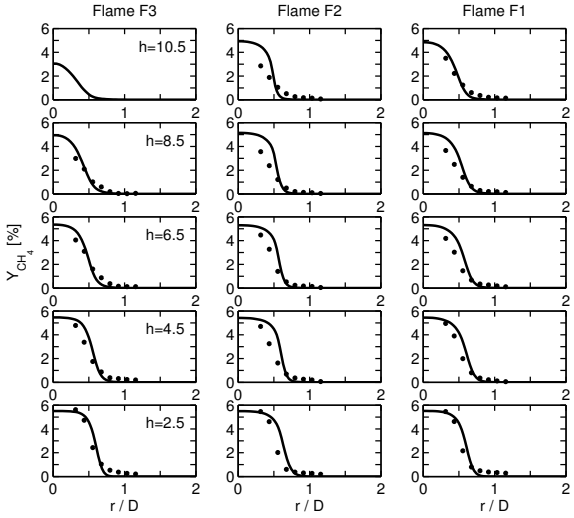

Figure 7. Mean CH_4 mass fraction Y_{CH_4} in percent for the F3, F2, and F1 flames. Dots denote experimental results [8], and lines denote simulation results.

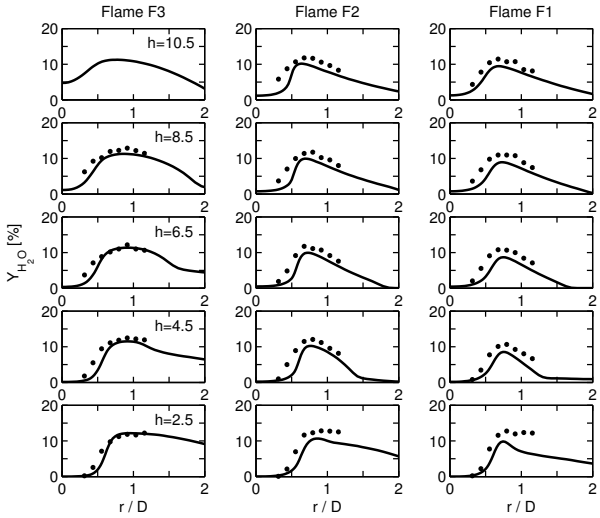

Figure 8. Mean H_2O mass fraction Y_{H_2O} in percent for the F3, F2, and F1 flames. Dots denote experimental results [8], and lines denote simulation results.

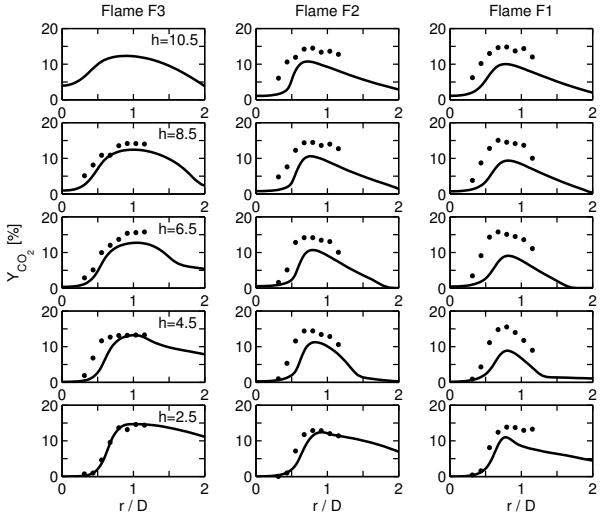

Figure 9. Mean CO_2 mass fraction Y_{CO_2} in percent for the F3, F2, and F1 flames. Dots denote experimental results [8], and lines denote simulation results.

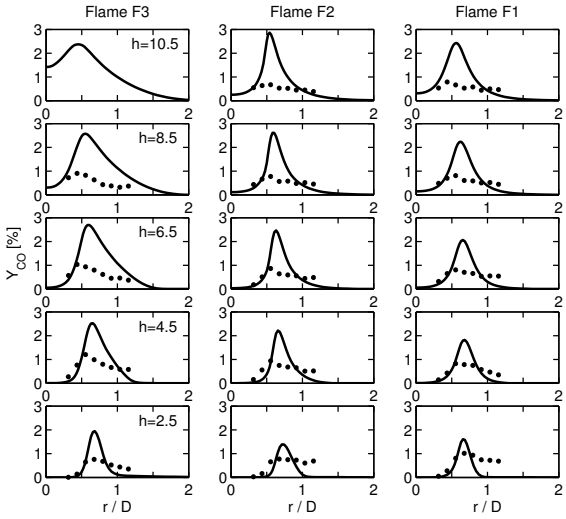

Figure 10. Mean CO mass fraction Y_{CO} in percent for the F3, F2, and F1 flames. Dots denote experimental results [8], and lines denote simulation results.

The CO overestimation in the F3 flame cannot be explained in such a way since the temperature and CO_2 levels are well predicted. Similar high CO levels have been reported by Lindstedt and Vaos [29]. The estimated error in the measurements of Chen et al. [8] regarding the minor species CO and OH is between 20% and 25%. Thus, the errors of measurements cannot explain the overpredictions of up to 100% which are observed in the simulations. Simulations with the full GRI 2.11 mechanism [58] do not improve the CO predictions (see the discussion of the influence of differently complex chemical mechanisms in the following paragraph). Given the relatively well predictions of all the other species it is unclear which reason may cause the observed discrepancy between CO measurements and simulation results.

Figure 11 shows results of the mean OH mass fraction Y_{OH}. The OH levels are well predicted for all the three flames for axial positions $h \leq 6.5$. This finding is somewhat unexpected regarding the F1 flame: its temperature is overpredicted for $h \leq 6.5$, and the OH-radical concentration is known to be very sensitive to temperature levels. Moreover, all the measurements of OH seem to indicate a broader flame region, which implies significant OH amounts in flame regions with very low mean temperatures. Similar results have been found by Lindstedt and Vaos [29]. They concluded that some caution may be required regarding the interpretation of the experimental data.

The influence of differently complex chemical mechanisms [5, 31] and finite-rate chemistry effects [28] on the predictions of transported PDF methods have been studied in previous investigations. Two different chemical mechanisms have been applied here to study the influence of the chemistry scheme: simulation results obtained with

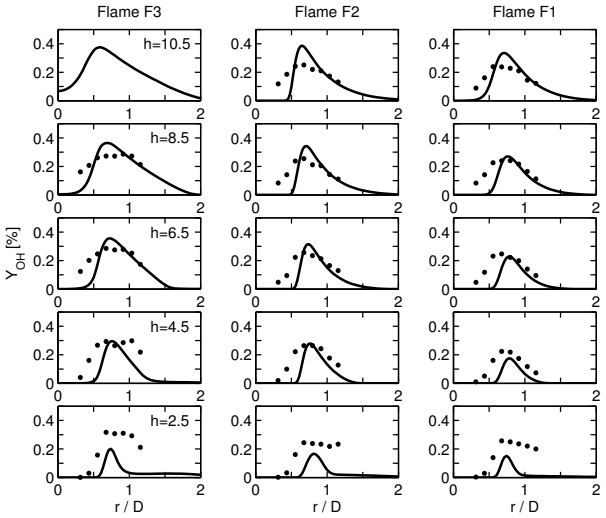

Figure 11. Mean OH mass fraction Y_{OH} in percent for the F3, F2, and F1 flames. Dots denote experimental results [8], and lines denote simulation results.

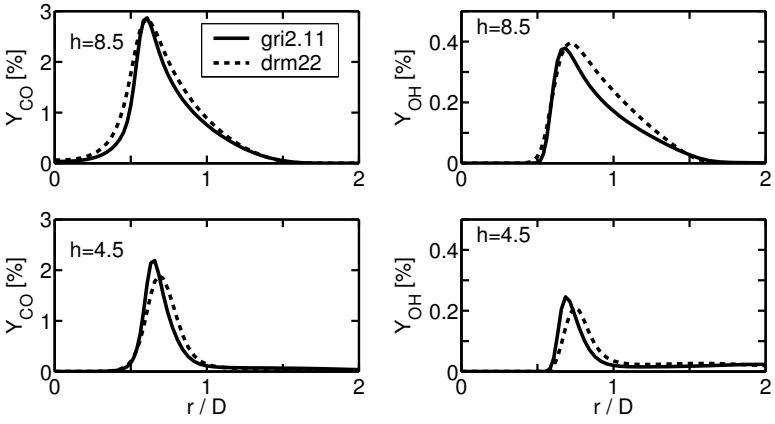

Figure 12. Comparison of simulation results for the F3 flame obtained with the GRI 2.11 mechanism (solid line) and the skeletal DRM22 mechanism (dashed line). The left column shows the CO mass fraction, and the right column shows the OH mass fraction. In both simulations, the mixing model (15) was used in combination with the GC model (24) for C_α.

the DRM22 [26] skeletal mechanism are compared in Figure 12 with results obtained with the full GRI 2.11 mechanism [58]. CO and OH mass fractions of F3 flame simulations are shown to address the overestimation of CO predictions and sensitivity of the OH-radical concentration: see the discussion in the preceding paragraph. In both F3 flame simulations, the mixing model (15) was used in combination with the GC model (24) for C_α. One observes that the results obtained with the different mechanisms are almost identical. This fact indicates that the simplifications used to obtain the skeletal mechanism DRM22 do not affect the simulation results.

7. Comparison with other scalar mixing frequency models

After demonstrating the good performance of the GC model in flame simulations, let us compare the GC model with other ω_α models for premixed turbulent combustion. First, previously developed ω_α models [6, 29, 38] will be described to explain the underlying assumptions of these models. Second, flame calculations involving such other ω_α models will be compared to predictions based on the GC model.

An alternative approach to the direct derivation of models for the scalar mixing frequency ω_α is to consider a transport equation for the scalar dissipation rate ε_α. The relation between ε_α and ω_α provided by the expressions (9) and (15) is given by

$$\omega_\alpha \overline{\phi_\alpha''^2} = \varepsilon_\alpha + \frac{\overline{\nu}}{Sc_\alpha} \frac{\partial \overline{\phi}_\alpha}{\partial x_k} \frac{\partial \overline{\phi}_\alpha}{\partial x_k}. \tag{34}$$

Usually, the relatively small last contribution in (34) is neglected in these approaches (which corresponds to the assumption of high Reynolds numbers) such that ω_α is given by $\omega_\alpha = \varepsilon_\alpha / \overline{\phi_\alpha''^2}$. Transport equations for the scalar dissipation rate have been proposed, for example, by Zeman and Lumley [63], Jones and Musonge [25], Mantel and Borghi [30] and Mura and Borghi [38]. The structure of scalar dissipation rate models [13, 54] can be illustrated by the model of Mura and Borghi [38], which is applicable to premixed turbulent combustion. The latter model is given by

$$\begin{aligned} \frac{\partial \langle\rho\rangle \varepsilon_\alpha^{MB}}{\partial t} + \frac{\partial \langle\rho\rangle (\overline{u}_k - \overline{U}_{L_k}) \varepsilon_\alpha^{MB}}{\partial x_k} - \frac{\partial}{\partial x_k} \left(\langle\rho\rangle D_t \frac{\partial \varepsilon_\alpha^{MB}}{\partial x_k} \right) \\ = \left(c_\alpha \frac{\varepsilon}{k} \frac{P_\alpha'}{\varepsilon_\alpha^{MB}} + c_U \frac{\varepsilon}{k} \frac{P}{\varepsilon} + \alpha \frac{\varepsilon}{k} - \beta' \frac{\varepsilon_\alpha^{MB}}{\overline{\phi_\alpha''^2}} \right) \langle\rho\rangle \varepsilon_\alpha^{MB}. \end{aligned} \tag{35}$$

The model (35) was derived on the basis of flamelet assumptions for infinitely high Damköhler numbers. The source terms on the right-hand side are related to the production and dissipation terms that appear in transport equations for the turbulent kinetic energy and scalar variances. In particular, the production P by large-scale velocity fields and the production P_α' by large-scale scalar fields are given by

$$P = \nu_t \frac{\partial \overline{u}_k}{\partial x_k} \frac{\partial \overline{u}_k}{\partial x_k}, \quad P_\alpha' = \frac{\nu_t}{Sc_t} \frac{\partial \overline{\phi}_\alpha}{\partial x_k} \frac{\partial \overline{\phi}_\alpha}{\partial x_k}. \tag{36}$$

The diffusion coefficient is given by $D_t = \nu_t / Sc_{\varepsilon_\alpha}$, where Sc_{ε_α} refers to the turbulent Schmidt number in the ε_α equation. The propagation term $\overline{U}_{L_k}$ of flamelets and the parameter $\beta^{'}$ are given by

$$\overline{U}_{L_k} = \frac{S_L}{1+\sqrt{2k/3}/S_L} \frac{\partial \overline{\phi}_\alpha}{\partial x_k} \left(\frac{\partial \overline{\phi}_\alpha}{\partial x_j} \frac{\partial \overline{\phi}_\alpha}{\partial x_j} \right)^{-\frac{1}{2}}, \quad \beta^{'} = \beta \left(1 - \frac{2}{3} c_{\varepsilon_\alpha} \frac{S_L}{\sqrt{k}} \right). \quad (37)$$

Here, S_L is the laminar burning velocity of the mixture. The model constants are given by $\alpha = 0.9$, $\beta = 4.2$, $c_U = c_\alpha = 1.0$, $c_{\varepsilon_\alpha} = 0.1$ and $Sc_{\varepsilon_\alpha} = 1.3$ [60]. The model (35) will be referred to below as Mura and Borghi (MB) model. It is worth noting, however, that there are some questions related to the MB model. The reaction contributions in the MB model are given by the flamelet propagation velocity $\overline{U}_{L_k}$ and the term $2/3 c_{\varepsilon_\alpha} S_L / \sqrt{k}$ in the expression for the $\beta^{'}$ coefficient. To see the importance of the flamelet propagation as compared to the fluid velocity we consider the ratio $Z = \sqrt{\overline{U}_{L_k} \overline{U}_{L_k}} / \sqrt{\overline{u_k} \overline{u_k}}$ between the magnitude of the flamelet propagation velocity and the magnitude of the fluid velocity.

Figure 13 shows the values of the ratio Z and the term $2/3 c_{\varepsilon_\alpha} S_L / \sqrt{k}$ along the mean flame front position (see the definition below) for the F3 flame. The ratio Z remains less than 0.01 for most parts of the flame. Hence, the influence of the flamelet propagation velocity is negligible. The factor $2/3 c_{\varepsilon_\alpha} S_L / \sqrt{k}$ is less than 0.02, which implies that $\beta' \approx \beta$. The two reactive contributions Z and $2/3 c_{\varepsilon_\alpha} S_L / \sqrt{k}$ are even smaller for the F2 and F1 flames (not shown) since the fluid velocity and the turbulence levels are much higher in these flames. Thus, the MB model (35) reduces to a transport equation for a passive scalar regarding the flames considered. The latter cannot be seen to be justified since the fuel mass fraction (which was used for the calculation of the scalar dissipation rate) is a highly reactive scalar. It is interesting to compare the MB

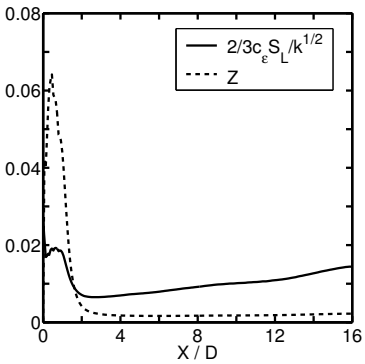

Figure 13. Reaction contributions $2/3 c_{\varepsilon_\alpha} S_L / \sqrt{k}$ and $Z = \sqrt{\overline{U}_{L_k} \overline{U}_{L_k}} / \sqrt{\overline{u_k} \overline{u_k}}$ in the MB model (35) for the F3 flame along the mean flame front.

model for non-reacting scalars (this means for $\overline{U}_{L_k} = 0$ and $\beta^{'} = \beta$) with the model of Jones and Musonge [25] and a variety of other scalar dissipation rate equations studied by Sanders and Goekalb [54]. This comparison reveals a significant difference between the MB model and other models for the scalar dissipation rate: the $\alpha\,\varepsilon/k$ term acts as a production term in equation (35) whereas the corresponding term in the model of Jones and Musonge [25] represents a sink term. Thus, the MB model disagrees with many other models for the scalar dissipation rate of non-reacting scalars.

The underlying assumptions related to the algebraic scalar frequency model of Lindstedt and Vaos [29] can be seen by taking reference to the algebraic version of the MB model. By assuming that the evolution of the scalar dissipation rate is dominated by the source terms on the right-hand side, equation (35) implies an algebraic expression for the scalar mixing frequency $\omega_\alpha = \varepsilon_\alpha/\widetilde{\phi_\alpha^{''2}}$,

$$\omega_\alpha = \frac{1}{\beta\left(1 - \frac{2}{3}c_{\varepsilon_\alpha}S_L/\sqrt{k}\right)}\left(c_\alpha\frac{P_\alpha^{'}}{\varepsilon_\alpha} + c_U\frac{P}{\varepsilon} + \alpha\right)\frac{\varepsilon}{k}. \tag{38}$$

The use of the first-order Taylor series approximation for the chemical reaction contribution then results in

$$\omega_\alpha = \frac{C_\alpha^{'}}{2}\left(1 + \frac{2}{3}c_{\varepsilon_\alpha}\frac{S_L}{\sqrt{k}}\right)\frac{\varepsilon}{k}, \tag{39}$$

where $C_\alpha^{'} = 2(c_\alpha P_\alpha^{'}/\varepsilon_\alpha + c_U P/\varepsilon + \alpha)/\beta$ denotes a mixing parameter. Kuan et al. [27] and Lindstedt and Vaos [29] derived an expression for ω_α which is similar to expression (39). Their scalar mixing frequency model is given by

$$\omega_\alpha^{LV} = \frac{C_\alpha^{'}}{2}\left(1 + C_\alpha^{*}\frac{\rho_u}{\langle\rho\rangle}\frac{S_L}{v_k}\right)\frac{\varepsilon}{k}. \tag{40}$$

Here, $C_\alpha^{'} = 4$ and $C_\alpha^{*} = 1.2$ are model constants [29]. ρ_u denotes the density of the unburned mixture, $\langle\rho\rangle$ is the mean mass density, and v_k is the Kolmogorov velocity. The essential assumption related to the Lindstedt and Vaos (LV) model (40) is given by the consideration of $C_\alpha^{'}$ as a constant, which corresponds to the idea of velocity and scalar fields that are characterized by a local equilibrium between production and dissipation ($P_\alpha^{'}/\varepsilon_\alpha$ and P/ε are constant). This condition is not satisfied regarding the flames considered here. Figure 14 shows radial profiles of the scalar production-to-dissipation ratio $P_\alpha^{'}/\varepsilon_\alpha$ and the turbulence production-to-dissipation ratio P/ε in F3 flame simulations. As can be seen, the profiles of the production-to-dissipation ratios vary significantly at both axial positions. Hence, the scalar production-to-dissipation ratio $P_\alpha^{'}/\varepsilon_\alpha$ and the turbulence production-to-dissipation ratio P/ε are far from being constants. Similar results have been found regarding the F2 and F1 flames (not shown). It is also worth noting that the inclusion of the effect of chemical reactions differs from expression (39), in particular, by the use of the Kolmogorov velocity v_k instead of $\sqrt{k}$.

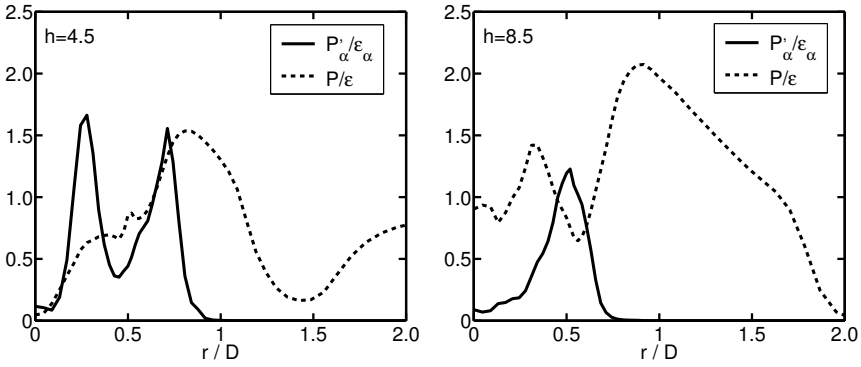

Figure 14. Radial profiles of the scalar production-to-dissipation ratio $P'_\alpha/\varepsilon_\alpha$ (solid line) and the turbulence production-to-dissipation ratio P/ε (dashed line) in F3 flame simulations. The results have been obtained by adopting the GC model.

An alternative suggestion for the algebraic modeling of the scalar mixing frequency was made by Cha and Trouillet [6]. Their model relies on the assumption that the large-scale turbulent motions control the scalar mixing frequency (the mixing frequency of reacting scalars is related to the mixing frequency of non-reacting scalars). However, Cha and Trouillet's model was developed for non-premixed turbulent flames. Thus, it will be not considered for comparisons here.

The simplest ω_α model is recovered by neglecting chemistry effects in the LV model,

$$\omega_\alpha^{ST} = \frac{C_\alpha}{2}\frac{\varepsilon}{k}. \tag{41}$$

The model (41) will be referred to below as standard (ST-*) scalar mixing frequency model, where * refers to the constant value of C_α applied. The basic assumption related to the model (41) is that the scalar mixing frequency ω_α is controlled by the mixing frequency $\omega = \varepsilon/k = 1/\tau$ of large-scale turbulent motions. Let us have a closer look at the validity of this assumption. Figure 15 shows radial profiles of the normalized scalar mixing frequency $\omega_\alpha\tau_c$, the normalized turbulence frequency $\omega\tau_c$, and the normalized Kolmogorov frequency $\omega_\eta\tau_c$ at axial positions $h = 4.5$ and $h = 8.5$ for the F3 and F1 flames. Here, the Kolmogorov frequency ω_η is defined by $\omega_\eta = (\varepsilon/\overline{\nu})^{1/2}$. The frequency values have been normalized by the chemical time scale $\tau_c = 0.44$ ms which is defined as ratio of the laminar flame thickness and laminar burning velocity [8]. High values of the normalized scalar mixing frequency are found within the turbulent flame brush. The reason for that is given by the three terms involved in A_α (see relation (22)). The correlation $\overline{S''_\alpha \phi''_\alpha}$ between scalar mixing and chemical reactions increases the scalar mixing frequency directly. The rapid consumption of the fuel in the premixed flame steepens the gradients of the scalar mean and variance. The steep

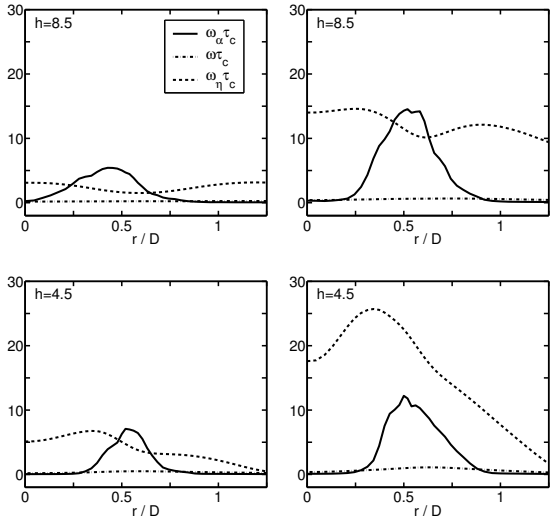

Figure 15. Radial profiles of the normalized scalar mixing frequency $\omega_\alpha \tau_c$ (solid line), the normalized turbulence frequency $\omega \tau_c$ (dashed-dotted line) and the normalized Kolmogorov frequency $\omega_\eta \tau_c$ (dashed line) for the F3 and F1 flames. The frequency values have been normalized by the chemical time scale $\tau_c = 0.44$ ms.

gradients then enhance the scalar mixing by increasing the two contributions in addition to $\overline{S''_\alpha \phi''_\alpha}$ in A_α. Figure 15 shows that the Kolmogorov frequency is larger than the scalar mixing frequency in the F1 flame at $h = 4.5$. Therefore, Kolmogorov scale eddies are able to enter and thicken the flame. This broadening was also reported in the experimental study of Chen et al. [8]. In the F3 flame the Kolmogorov frequency is found to be smaller than the scalar mixing frequency, which indicates a flamelet-type combustion. The turbulence frequency is much smaller than the scalar mixing frequency in the turbulent flame brush of both flames. The latter finding clearly shows that large-scale turbulent motions do not control the scalar mixing in these regions, this means the basic assumption of the model (41) is not satisfied for the flows considered. This conclusion is in consistency with O'Young and Bilger's [43] experimental investigations of premixed flames. The authors found that the ratio between the turbulence frequency and scalar mixing frequency varies over almost an order of magnitude.

To see the differences to predictions based on the GC model, simulations of the F3, F2, and F1 flames have been performed by adopting the MB model, the LV model, and the ST-6 model (in accord with the observations of Lindstedt and Vaos [29] it was found that the combination of the ST-* model with $C_\alpha = 6$ represents an optimal choice). It turned out that the MB model combined with $\beta = 4.2$ did not allow calculations of stably burning F3, F2, and F1 flames. Thus, the MB model was used in con-

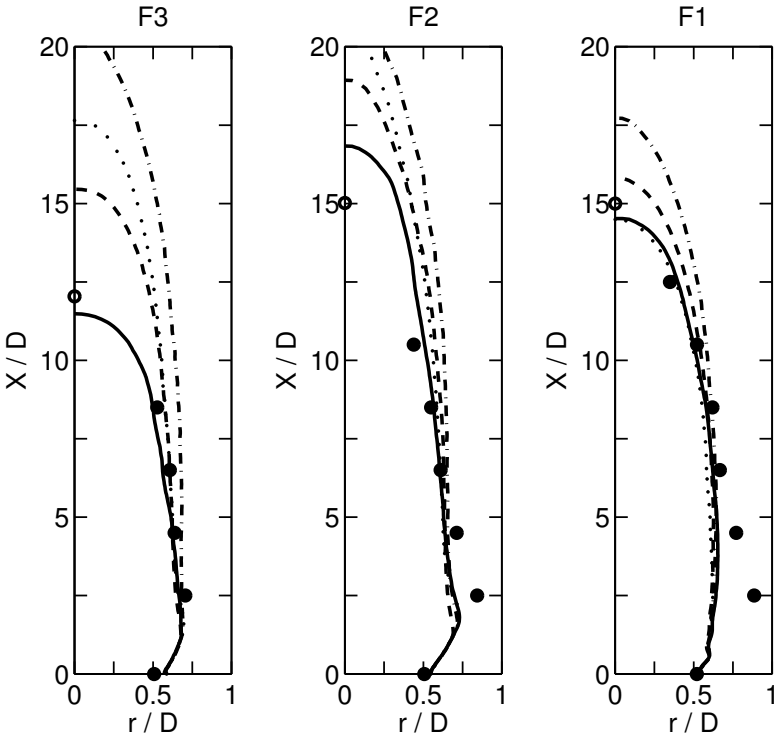

Figure 16. Position of the mean turbulent flame front obtained in F3, F2, and F1 flame simulations by different scalar mixing frequency models: GC model (solid line), MB model (dotted line), LV model (dashed line), ST-6 model (dashed-dotted line). Dots denote experimental results. The circles denote curve fit results to the measured values [8]. The iso-line temperatures are $\overline{T}_1 = 1300\,\mathrm{K}$ for the F1 flame, $\overline{T}_2 = 1400\,\mathrm{K}$ for the F2 flame, and $\overline{T}_3 = 1500\,\mathrm{K}$ for the F3 flame respectively.

junction with $\beta = 0.3$, which provided the best agreement between simulation results and measurements. Results obtained with the different frequency models are compared with experimental data in Figure 16. This figure shows the mean flame front position which is defined as iso-line of the mean temperature. The iso-line temperatures are $\overline{T}_1 = 1300\,\mathrm{K}$ for the F1 flame, $\overline{T}_2 = 1400\,\mathrm{K}$ for the F2 flame, and $\overline{T}_3 = 1500\,\mathrm{K}$ for the F3 flame respectively. The mean flame front position predicted by the GC frequency model agrees well with the measured positions for all three flames. Thus, the GC frequency model provides very good predictions for a range of combustion regimes. The use of the MB model, LV model and ST-6 model results in significant overestimations of the axial position of the flame tip regarding the F3 and F2 flames.

In the flame tip, the turbulent burning velocity has to balance the high axial velocity of the jet. Thus, predictions of the axial position of the flame tip are very sensitive to an accurate prediction of the turbulent burning velocity. In the F3 and F2 flames, which are close to the flamelet regime, one finds strong axial gradients of mean scalars and scalar variances in the flame tip. These gradients increase the scalar mixing frequency (i.e., the mixing efficiency), which leads to an increase of the turbulent burning velocity. The GC frequency model includes the effects of the strong gradients of scalar means and variances in the flame tip such that the GC model provides an accurate prediction of the flame tip position. In contrast to that, the ST-6 model and the LV model do not include any effects of mean scalar and scalar variance gradients on the scalar mixing. These models underestimate, therefore, the turbulent burning velocity, which explains the overestimation of the flame tip position. The overprediction of the flame tip position observed in the MB model simulations probably results from the underestimation of the chemical reaction contributions (see the discussion above). Regarding the mean flame front position in F1 flame simulations one finds (with the exception of the ST-6 model) that the predictions of the different mixing frequency models agree well with the measurements. The F1 flame is closer to the well-stirred combustion regime such that the scalar gradients are not as strong as in the F3 and F2 flames. The mixing enhancement is less intense, which explains the close agreement of results.

Figure 17 shows normalized mixing frequencies in F3 flame simulations according to the four scalar frequency models considered. Figure 18 shows the corresponding values of the mixing coefficient C_α. The GC model and the MB model display a peak of the scalar mixing frequency. At both axial positions the peak predicted by the MB model is located further outward than the peak predicted by the GC model. How can this observation explain the different results for the mean flame front position? In an analogy to a 1-d laminar flame the turbulent flame brush can be divided into a preheat zone (fresh gas side of the flame front) and a reaction zone (burnt gas side of the flame front). The peak value of the scalar mixing frequency predicted by the GC model is then located in the preheat zone and the peak predicted by the MB model is located in the reaction zone of the turbulent flame brush. The preheat zone is the zone where the temperature of the fresh mixture is increased due to convection and diffusion of heat from the reaction zone where most of the chemical reactions and the heat release take place. High values of the scalar mixing frequency in the preheat zone allow for a faster mixing of the temperature and thereby reactions can take place at further inward radial locations. Without enhanced mixing in the preheat zone the location of the reaction zone will be located further outward. Due to the heat release the location of the reaction zone determines the mean flame front position. Therefore, one would expect that the mean flame front position predicted by the GC model is located further inward than the position predicted by the MB model. Exactly this feature can be seen in Figure 16. The scalar mixing frequencies obtained with the ST-6 model and the LV model differ significantly from the values predicted by the GC model and the MB

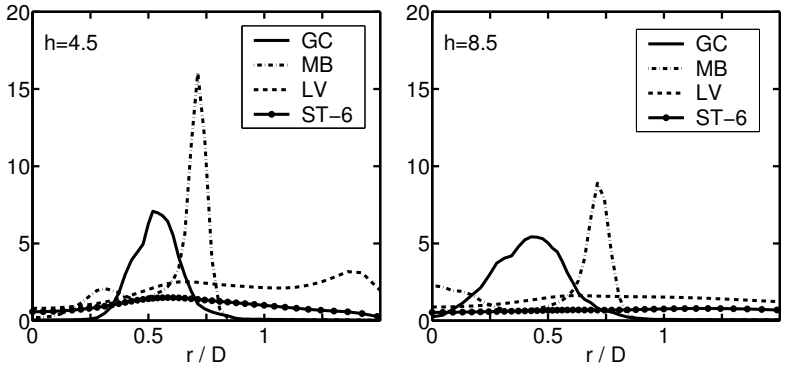

Figure 17. Radial profiles of the normalized scalar mixing frequency $\omega_\alpha \tau_c$ obtained in F3 flame simulations by the GC model (solid line), the MB model (dashed line), the LV model (dashed-dotted line) and the ST-6 model (dotted line). The frequency values have been normalized by the chemical time scale $\tau_c = 0.44\,\text{ms}$.

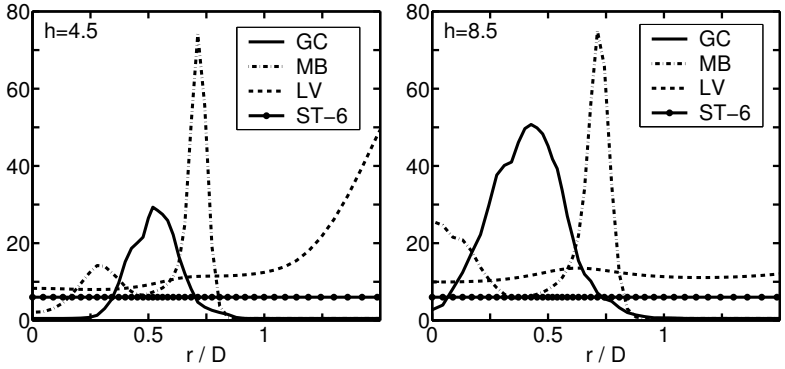

Figure 18. Radial profiles of the scalar mixing coefficient C_α obtained in F3 flame simulations by the GC model (solid line), the MB model (dashed line), the LV model (dashed-dotted line) and the ST-6 model (dotted line).

model: these scalar mixing frequency profiles are rather flat, and they do hardly show a peak. The latter behavior results from the fact that both models do not account for mean scalar and scalar variance gradients. As can be seen in Figure 18 the LV model predicts unreasonably high values for the mixing parameter C_α in the outer part of the flame at the position $x/D = 4.5$. This part of the flame corresponds to the burnt gas side of a 1-d laminar flame which is dominated by convection of the hot gases. The high values result from the reaction contribution in the LV model (40): small values of the Kolmogorov velocity v_k due to the high values of molecular viscosity and small values of the mean density $\langle\rho\rangle$ (both are caused by the high temperature) result in high values of the ratio $\frac{\rho_u}{\langle\rho\rangle}\frac{S_L}{v_k}$.

8. Summary

Previously developed PDF methods for premixed turbulent combustion were considered in detail in Section 7. This discussion revealed significant problems of existing approaches to model the scalar mixing frequency: the assumptions applied are not justified in general (see the discussion related to the LV and ST-* models) or they are in disagreement with other modeling efforts (see the discussion of the MB model). The GC frequency model was introduced here as an alternative to these existing PDF methods for premixed turbulent combustion. The modeling concept applied is relatively general: the GC model is constructed such that deviations of a local equilibrium between production processes and dissipation of scalar variances become minimal. This concept offers significant conceptual advantages compared to existing methods. Empirical parametrizations are not involved, there is no need to adjust several model parameters to the flow considered, and effects of chemical reactions on scalar mixing frequencies are involved without making assumptions that have an uncertain range of applicability. It is also worth noting that the computational effort required to take advantage of the GC frequency model is reasonable. Compared to the LV model, for example, the increase of computational costs is given by a factor of about 1.2.

The suitability of the GC scalar frequency model was demonstrated by applications to several turbulent premixed Bunsen flames that cover various regimes ranging from flamelet to distributed combustion. Comparisons with existing scalar mixing frequency models for premixed turbulent combustion revealed the advantages of the GC frequency model. The main reason for these advantages is the following one. Existing scalar mixing frequency models are constructed on the basis of the idea to implement chemical reaction effects explicitly in equations for non-reacting scalars. However, the studies reported here show that chemical reactions also have a significant implicit effect on the scalar mixing frequency: a relatively small flame thickness due to the fast chemistry implies significant gradients of scalar means and variances. The GC frequency model relates the relatively small flame thickness to a relatively small scalar mixing time scale (a relatively high scalar frequency) via the increase of gradients of

scalar means and variances. This important effect is correctly represented in the GC frequency model which explains its success.

Many real flames involve a variety of mixing regimes (non-premixed, partially-premixed and premixed turbulent combustion). A significant advantage of the approach presented here is given by its applicability to such flames involving several combustion regimes. Obviously, such applications will be very valuable for the further evaluation of the capabilities of the approach presented. Questions that need further investigations concern, for example, the relevance of using more complex scalar mixing models and the relevance of using specific scalar mixing frequencies for different species. It is worth noting that essentially the same scalar modeling approach can be used to enable hybrid LES/FDF calculations.

Acknowledgments. This work has been supported by the German Research Foundation (DFG) and Fluent Inc. (DFG Transfer Project 42). In particular, we are very thankful to Dr. M. Braun (Fluent Germany) and Professor R. Friedrich for significant support regarding the realization of this project. The authors gratefully acknowledge valuable support of Dr. G. Goldin (Fluent USA) regarding the realization of computations. We are very thankful to Professor P. Jenny for many helpful comments on our work. The computational resources have been provided by the Institute of Scientific Computation (ISC) at the University of Wyoming.

References

1. J. Abraham, F. A. Williams and F. V. Bracco, A discussion of turbulent flame structure in premixed charges, *SAE Paper* **850345** (1985).
2. M. S. Anand and S. B. Pope, Calculations of premixed turbulent flames by PDF methods, *Combustion and Flame* **67** (1987), pp. 127–142.
3. R. Borghi, Turbulent combustion modelling, *Progress in Energy and Combustion Science* **14** (1988), pp. 245–292.
4. R. R. Cao and S. B. Pope, Numerical integration of stochastic differential equations: Weak second-order mid-point scheme for application in the composition PDF method, *Journal of Computational Physics* **185** (2003), pp. 194–212.
5. _____, The influence of chemical mechanisms on PDF calculations of nonpremixed piloted jet flames, *Combustion and Flame* **143** (2005), pp. 450–470.
6. C. M. Cha and P. Trouillet, A model for the mixing time scale of a turbulent reacting scalar, *Physics of Fluids* **15** (2003), pp. 1375–1380.
7. _____, A subgrid-scale mixing model for large eddy simulations of turbulent reacting flows using the filtered density function, *Physics of Fluids* **15** (2003), pp. 1496–1504.
8. Y. C. Chen, N. Peters, G. A. Schneemann, N. Wruck, U. Renz and M. S. Mansour, The detailed flame structure of highly stretched turbulent premixed methane-air flames, *Combustion and Flame* **107** (1996), pp. 223–244.
9. P. J. Colucci, F. A. Jaberi, P. Givi and S. B. Pope, Filtered density function for large eddy simulation of turbulent reacting flows, *Physics of Fluids* **10** (1998), pp. 499–515.

10. C. Dopazo, Recent development in PDF methods, in: *Turbulent Reacting Flows* (P. A. Libby and F. A. Williams, eds.), pp. 375–474, Academic, New York, 1994.

11. C. Dopazo and E. E. O'Brien, An approach to autoignition of a turbulent mixture, *Acta Astronautica* **1** (1974), pp. 1239–1266.

12. FLUENT, *6.3 User Guide*, FLUENT INC., Lebanon, NH, 2006.

13. R. O. Fox, *Computational Models for Turbulent Reacting Flows*, Cambridge University Press, Cambridge, UK, 2003.

14. F. Gao and E. E. O'Brien, A large eddy simulation scheme for turbulent reacting flows, *Physics of Fluids* **A5** (1993), pp. 1282–1284.

15. L. Y. M. Gicquel, P. Givi, F. A. Jaberi and S. B. Pope, Velocity filtered density function for large eddy simulation of turbulent flows, *Physics of Fluids* **14** (2002), pp. 1196–1213.

16. P. Givi, Filtered density function for subgrid scale modeling of turbulent combustion, *AIAA Journal* **44** (2006), pp. 16–23.

17. S. Heinz, On Fokker-Planck equations for turbulent reacting flows. Part 1. Probability density function for Reynolds-averaged Navier-Stokes equations, *Flow, Turbulence and Combustion* **70** (2003), pp. 115–152.

18. _____, On Fokker-Planck equations for turbulent reacting flows. Part 2. Filter density function for large eddy simulation, *Flow, Turbulence and Combustion* **70** (2003), pp. 153–181.

19. _____, *Statistical Mechanics of Turbulent Flows*, Springer-Verlag, Berlin, 2003.

20. _____, Unified turbulence models for LES and RANS, FDF and PDF simulations, *Theoretical and Computational Fluid Dynamics* **21** (2007), pp. 99–118.

21. S. Heinz and D. Roekaerts, Reynolds number effects on mixing and reaction in a turbulent pipe flow, *Chemical Engineering Science* **56** (2001), pp. 3197–3210.

22. M. Herrmann, Numerical simulation of turbulent Bunsen flames with a level set flamelet model, *Combustion and Flame* **145** (2006), pp. 357–375.

23. J. Janicka, W. Kolbe and W. Kollmann, Closure of the transport-equation for the pobability density function of turbulent scalar fields, *Journal of Non-Equilibrium Thermodynamics* **4** (1979), pp. 47–66.

24. J. Janicka and A. Sadiki, Large eddy simulation of turbulent combustion systems, *Proceedings of the Combustion Institute* **30** (2005), pp. 537–547.

25. W. P. Jones and P. Musonge, Closure of the Reynolds stress and scalar flux equations, *Physics of Fluids* **32** (1988), pp. 3589–3604.

26. A. Kazakov and M. Frenklach, *DRM22*, `http://www.me.berkeley.edu/drm/`.

27. T. S. Kuan, R. P. Lindstedt and E. M. Vaos, in: *Advances in Confined Detonations and Pulse Detonation Engines* (G. Roy, ed.), pp. 17–40, Torus Press, Moscow, 2003, ISBN 5-94588-012-4.

28. R. P. Lindstedt, S. A. Louloudi, J. J. Driscoll and V. Sick, Finite rate chemistry effects in turbulent reacting flows, *Flow, Turbulence and Combustion* **72** (2004), pp. 407–426.

29. R. P. Lindstedt and E. M. Vaos, Transported PDF modeling of high-Reynolds-number premixed turbulent flames, *Combustion and Flame* **145** (2006), pp. 495–511.

30. T. Mantel and R. Borghi, A new model of premixed wrinkeled flame propagation based on a scalar dissipation equation, *Combustion and Flame* **96** (1994), pp. 443–457.

31. A. R. Masri, R. Cao, S. B. Pope and G. M. Goldin, PDF calculations of turbulent lifted flames of H_2/N_2 fuel issuing into a vitiated co-flow, *Combustion Theory and Modeling* **8** (2004), pp. 1–22.

32. B. Merci, B. Naud and D. Roekaerts, Flow and mixing fields for transported scalar PDF simulations of a piloted jet diffusion flame ("Delft Flame III"), *Flow, Turbulence and Combustion* **74** (2005), pp. 239–272.

33. _____, Interaction between chemistry and micro-mixing modeling in transported PDF simulations of turbulent non-premixed flames, *Combustion Science and Technology* **179** (2006), pp. 153–172.

34. B. Merci, D. Roekaerts and B. Naud, Study of the performance of three micro-mixing models in transported scalar PDF simulations of a piloted jet diffusion flame ("Delft Flame III"), *Combustion and Flame* **144** (2006), pp. 476–493.

35. B. Merci, D. Roekaerts, B. Naud and S. B. Pope, Study of the performance of different micro-mixing models in transported scalar PDF simulations of a piloted jet diffusion flame, *Combustion and Flame* **146** (2006), pp. 109–130.

36. D. W. Meyer and P. Jenny, A mixing model for turbulent flows based on parametrized scalar profiles, *Physics of Fluids* **18** (2006), pp. 035105/1–15.

37. S. Mitarai, J. J. Riley and G. Kosály, Testing of mixing models for Monte Carlo probability density function simulations, *Physics of Fluids* **17** (2005), pp. 047101/1–15.

38. A. Mura and R. Borghi, Towards an extended scalar dissipation equation for turbulent premixed combustion, *Combustion and Flame* **133** (2003), pp. 193–196.

39. A. Mura, F. Galzin and R. Borghi, A unified PDF-flamelet model for turbulent premixed combustion, *Combustion Science and Technology* **175** (2003), pp. 1573–1609.

40. M. Muradoglu and S. B. Pope, Local time-stepping algorithm for solving the probability density function turbulence model equations, *AIAA Journal* **40** (2002), pp. 1755–1763.

41. E. E. O'Brien, The probability density function (PDF) approach to reacting turbulent flows, in: *Turbulent Reacting Flows* (P. A. Libby and F. A. Williams, eds.), pp. 185–218, Springer-Verlag, Berlin, 1980.

42. M. R. Overholt and S. B. Pope, Direct numerical simulation of a passive scalar with imposed mean gradient in isotropic turbulence, *Physics of Fluids* **8** (1996), pp. 3128–3148.

43. F. O'Young and R. W. Bilger, Scalar gradient and related quantities in turbulent premixed flames, *Combustion and Flame* **109** (1997), pp. 682–700.

44. N. Peters, Laminar flamelet concepts in turbulent combustion, *21st Symposium (Int.) on Combustion, The Combustion Institute* (1986), pp. 1231–1250, Pittsburgh.

45. _____, *Turbulent Combustion*, Cambridge University Press, Cambridge, UK, 2000.

46. H. Pitsch and L. D. De Lageneste, Large eddy simulation of premixed turbulent combustion using a level-set approach, *Proceedings of the Combustion Institute* **29** (2002), pp. 2001–2008.

47. T. P. Poinsot and D. Veynante, *Theoretical and Numerical Combustion*, Second ed, Edwards, Philadelphia, 2005.

48. S. B. Pope, PDF methods for turbulent reactive flows, *Progress in Energy and Combustion Science* **11** (1985), pp. 119–192.

49. _____, Turbulent premixed flames, *Annual Review of Fluid Mechanics* **19** (1987), pp. 237–270.

50. _____, Computationally efficient implementation of combustion chemistry using a *in situ* adaptive tabulation, *Combustion Theory and Modelling* **1** (1997), pp. 41–63.

51. _____, *Turbulent Flows*, Cambridge Univerity Press, Cambridge, UK, 2000.

52. R. O. S. Prasad and J. P. Gore, An evaluation of flame surface density models for turbulent premixed jet flames, *Combustion and Flame* **116** (1998), pp. 1–14.

53. V. Raman, H. Pitsch and R. Fox, Hybrid large eddy simulation/Lagrangian filtered-density-function approach for simulating turbulent combustion, *Combustion and Flame* **143** (2005), pp. 56–78.

54. J. P. H. Sanders and I. Goekalp, Scalar dissipation rate modelling in variable density turbulent axisymmetric jets and diffusion flames, *Physics of Fluids* **10** (1998), pp. 938–948.

55. M. R. H. Sheikhi, T. G. Drozda, P. Givi, F. A. Jaberi and S. B. Pope, Large eddy simulation of a turbulent nonpremixed piloted methane jet flame (Sandia flame D), *Proceedings of the Combustion Institute* **30** (2005), pp. 549–556.

56. M. R. H. Sheikhi, T. G. Drozda, P. Givi and S. B. Pope, Velocity-scalar filtered density function for large eddy simulation of turbulent flows, *Physics of Fluids* **15** (2003), pp. 2321–2337.

57. T. H. Shih, W. W. Liou, A. Shabbir, Z. Yang and J. Zhu, A new $k - \varepsilon$ eddy-viscosity model for high Reynolds number turbulent flows - Model development and validation, *Computers and Fluids* **24** (1995), pp. 227–238.

58. G. Smith, D. Golden and M. Frenklach, *Gri-Mech 2.11*, `http://www.me.berkeley.edu/grimech`.

59. S. Subramaniam and S. B. Pope, A mixing model for turbulent reactive flows based on Euclidean minimum spanning trees, *Combustion and Flame* **115** (1998), pp. 487–514.

60. N. Swaminathan and K. N. C. Bray, Effect of dilatation on scalar dissipation in turbulent premixed flames, *Combustion and Flame* **143** (2005), pp. 549–565.

61. J. Villermaux and J. C. Devillion, Represéntation de la coalescence et de la redispersion des domaines de ségrégation dans un fluide par un modéle d'interaction phénoménologique, *Proceedings of the Second International Symposium on Chemical Reaction Engineering* **ISCRE** (1972), pp. 1–13, New York.

62. J. Xu and S. B. Pope, PDF calculations of turbulent nonpremixed flames with local extinction, *Combustion and Flame* **123** (2000), pp. 281–307.

63. O. Zeman and J. L. Lumley, Modeling buoyancy driven mixed layers, *Journal of the Atmospheric Sciences* **33** (1976), pp. 1974–1988.

Received May 10, 2008; revised October 02, 2008

Author information

Michael Stöllinger, Department of Mathematics, University of Wyoming, 1000 East University Avenue, Laramie, WY 82071, USA.
Email: `mstoell@uwyo.edu`

Stefan Heinz, Department of Mathematics, University of Wyoming, 1000 East University Avenue, Laramie, WY 82071, USA.
Email: `heinz@uwyo.edu`